The Effect of Hydration on the Microstructural Properties of Individual Phases of Ordinary Portland Cement

Isabella Sharpley

Supervisor: Professor Ian Robinson

1st April 2015

A Dissertation submitted in part fulfillment for: Degree of MSci Physics:

Dept. Physics and Astronomy
University College London

ABSTRACT

Despite being the most abundant building material in the world, cement still poses questions regarding its exact composition and hydration properties. An investigation into the evolution of microstructural properties of OPC during hydration is presented. The hydration development in the pure phases, Calcium trisilicate (C_3S) and Calcium trialuminate (C_3A), is followed using the non-invasive method of x-ray powder diffraction. The average crystallite size and lattice micro-strain of each sample is monitored at regular time intervals over to a period of about 2 weeks via the Williamson Hall method. Careful monitoring of hydration products to deduce the hydration mechanism is done.

A null result was attained for the average lattice strain in the C_3A, and it's crystallite size varies throughout the time period but ultimately appears to remain constant throughout. The C_3S crystallite size shows an increase in strain during the initial rapid hydrolysis phase corresponding to a decrease in crystallite size. The C_3A is depleted by approximately 80% during the 16days of hydration while the C_3S shows a 30% decrease over 11 days.

The results confirm a dissolution along with nucleation and growth mechanism of hydration

ACKNOWLEDGMENTS

I would like to thank Professor Ian Robinson for his kind supervision throughout the project, Bo Chen for his continued assistance with sample preparation and Zhuo Feng for his help in the lab.

Glossary

- The following cement nomenclature will be used throughout the report:

C	Cao: Free lime
S	SiO_2: Silica
A	Al_2O_3: Alumina
F	Fe_2O_3: Iron oxide
H	H_20: water
C3S	$3CAO.SiO_2$ – alite – Tricalcium silicate
C2S	2CaO.SiO2 – Belite – Dicalcium silicate
C3A	3CaO. Al203 – Tricalcium aluminate
C4AF	4CaO.Al2O3. Fe2O3 - ferrite
CH	$Ca(OH)_2$ – Portlandite – Calcium hydroxide
C-S-H	Calcium Silicate Hydrate

- Abbreviations

PC	Portland cement
OPC	Ordinary Portland Cement
W/C	Water to Cement ratio
XRD	X-ray diffraction
XRPD	X-ray Powder Diffraction
SEM	Scanning electron microscopy
TEM	Transmission Electron Microscopy
S.A	Surface Area
W-H	Williamson Hall
FWHM	Full Width Half Maximum

Contents Page

1. Introduction

From the Egyptian pyramids, across Greek and roman times and throughout the middle ages [1] cement-based materials have been used for building structures throughout history. Cement paste (water and cement mix) binds together inert aggregate such as sand or crushed gravel forming concrete. Concrete based on PC is the most used material in the world (surpassed only by water) and has an annual production of 7 billion tons [2]. While intrinsically cement is low in energy to produce, due to its mass production, cement contributes 5-8% of CO_2 emissions annually and this is set to increase with developing countries expanding their infrastructure [3]. Therefore an improvement in the sustainability of cement is called for and in the future cement composition will likely need to be adjusted according to the locally available ingredients.

The durability and mechanical properties of cement are a direct consequence of the microstructure in which a pore network and the proximity of different hydration products play a key role [4]; therefore it is important to know what's going on at this level.

An understanding of cement at the microscopic level is essential for the development of enhanced and environmentally friendly cements, to be attained by the rationalization of cement properties; for example setting kinetics, strength development and hydration reactions which are altered by making changes to the composition of cement [5].

Cement is somewhat complex at the microstructural level and there remain unknowns particularly in relation to the hydration mechanism leading to the setting and hardening of cement, for which there are several different theories: A topo-chemical (solid state mechanism) in which the cement clinker liberates Ca^{2+} ions into solution upon initial contact with water. The calcium depleted unreacted clinker then reacts with this calcium rich solution producing hydration products. Versus a through-solution concept where the anhydrous grains dissolve and hydration products precipitate on the surface of grains[6].

Much research has been focused on the hydration of Portland cement as a whole, and there are many examples of XRPD studies reported on cement pastes [7].

The individual examination of pure phases will allow for a closer look at how the microstructural properties evolve and are affected during hydration, which will provide insight into a little piece of a big puzzle. The phases studied in this report are tri-calcium Aluminate and tri-calcium Silicate (which are the two most important phases controlling in terms of setting time and strength development during hydration), with the over all aim being to interpret changes in their physical properties - particularly crystallite size and lattice strain – over the course of hydration, by careful examination of measured x-ray diffraction patterns.

Objectives;

- To determine the effect of hydration on the microstructural properties of pure phases of OPC, by calculation of the average crystallite size and lattice strain of the water-cement phase system as a function of time since the moment of hydration.

- Careful monitoring of the formation of hydrates as a function of time to gauge the hydration mechanism.

The report is organized as follows: chapter 2 gives a broad overview of cement structure, hydration theories and the microstructural properties to be investigated.

Chapter 3 delves into the theoretical background of the X-ray diffraction technique and analysis methods employed

Chapter 4 is a description the experiment performed including and Chapter 5 contains the results and discussions of the findings; what it all means, suggested improvements and directions of future research.

2. Cement Structure and Hydration Chemistry

2.1 Cement composition and structure

The four major minerals that make up cement are alite, belite, aluminate and ferrite. In addition there exist a few minor phases i.e. calcium sulphate, alkali sulphates, and foreign oxides (Na_2O, K_2O, MgO, SiO_2, Al_2O_3, Fe_2O_3, TiO_2 and MnO_2) originating from the raw materials (limestone and clay) and fuel used during cement clinker production. [8].

Table 1: The main compounds of PC with Cement Chemistry Notation abbreviation (CNN) [9]

Mineral name	Compound name	Weight % (approx.)	Chemical Formula	Oxide composition	CNN
Alite	Tricalcium silicate	50-70	$Ca_3 \cdot SiO_5$	$3CaO \cdot SiO_2$	C_3S
Belite	Dicalcium silicate	25	$Ca_2 \cdot SiO_4$	$2CaO \cdot SiO_2$	C_2S
Aluminate	Tricalcium aluminate	10	$Ca_3 \cdot Al_2O_6$	$3CaO \cdot Al_2O_3$	C_3A
Ferite	Tetracalcium aluminoferrite	10	Ca_2AlFeO_5	$4CaO \cdot Al_2O_3 \cdot Fe_2O_3$	C_4aF

Although C_3A accounts for only 5-10% of the clinker composition by weight, due to it's high reactivity with water, it maintains a strong influence on the setting and hardening times of cement [8] and so understanding it's hydration is vital. Particularly as the main methods for future cement development involve increasing the level of aluminate [10]. Hence the role of C_3A and effect of its quantity on cement hydration is of increased interest.

The hydration of pure C_3A can lead to 'flash setting' - instantaneous setting - so in industry calcium sulphate in the form of gypsum is added to slow the reaction down and lengthen workability time.

Pure C_3A doesn't exhibit polymorphism. The $Ca_3Al_2O_6$ structure was first determined by Mondal and Jeffrey in 1975 [11] as cubic with lattice parameter a=1.5263nm, space group Pa3, Z=24 and characterized by Ca^{+2} atoms and rings of six AlO_4 tetrahedra [8].

Alite accounts for 50-70% of the clinker by mass and is known to dominate the early cement hydration reactions. It reacts relatively quickly in the presence of water and is the main phase responsible for early strength development in the first 28days [8]. exists as three different structures; triclinic, monoclinic and rhombohedral. At room temperature pure C_3S has a triclinic structural form. The first determination of it's structure was made by Jeffrey (1952) who showed that the polymorphs had similar structures and resolved a "pseudostructure" common to the three: they are pseudo-rhombohedral with lattice parameters a=b=~7.0Å, c=~25.0Å, space group R3m and Z=24 [12].

Belite accounts for 15-30% of the PC clinker and is less reactive than alite, contributing more to strength development beyond 28days. After a year the total contribution to strength obtained from alite and belite equalize when under similar conditions [8]. Ferrite makes up 5-15% of the clinker [8] and gives cement its distinctive grey colour. It is moderately reactive; initially reacting quickly with water but the reaction rate slows over time. The crystal structure of Ferrite, C_4AF, is complex. Ferrite is an approximation of the midpoint of the compositional series $Ca_2 (Al_xFe_{1-x})_2O_5$ [8].

2.2 Cement hydration

2.2.1 Hydration introduction

Hydration is responsible for the 'setting', which is the sudden loss of plasticity in the cement paste due to its conversion to solid material that occurs prior to the development of compressive strength during the 'hardening' (a much slower process) of cement. [13].

During hydration the minerals undergo a complex set of reactions that alter the chemical and physio-mechanical properties of the system and ultimately form hydrates by chemically bonding to water molecules. The W/C ratio used in concrete is typically 0.3-0.6 and greatly influences the resulting strength and workability of the concrete. A higher ratio gives lower strength due to an increase in the porosity created during the hydration process, but better workability (and vice versa) [14].

When trying to elucidate the hydration mechanism of PC, often the constituent phases are hydrated individually (as I will be doing) due to the complexity of the mix. In fact Le Chatelier found that the products produced on the hydration of cement are chemically identical to those formed by the hydration of the individual components under similar conditions. [15] This approach was used by Mindess and Young in 1981 [16] . However the products of hydration may influence each other or themselves interact with other components in the system, so the hydration of the individual components is more of an approximation to the real reactions .

2.2.2 C_3S hydration

C_3S hydrates relatively quickly, controlling the setting and hardening of OPC to a great extent. It's responsible for early strength development (first 7 days) and typically 70% of C_3S reacts in 28 days and nearly all of it in a year [14].

C_3S reacts with water, principally generating a poorly crystalline C-S-H gel and a lot of calcium hydroxide (also called portlandite, CH) as a secondary hydration product.[14]

$$2C_3S + 6H \rightarrow C_3S_2H_3 + 3CH \qquad (2.1)$$

The C-S-H composition varies over a wide range, while CH is a crystalline material with fixed composition.

The hydration of C_3S has been widely studied and there exist many theories existing on potential hydration mechanisms [17]. The hydration of C_3S (the main component) and hence cement generally, can be divided into five stages represented on the following calorimetry graph from Gartner et al [18].

Figure2.1 Calorimetry (heat evolution) graph of cement [18]

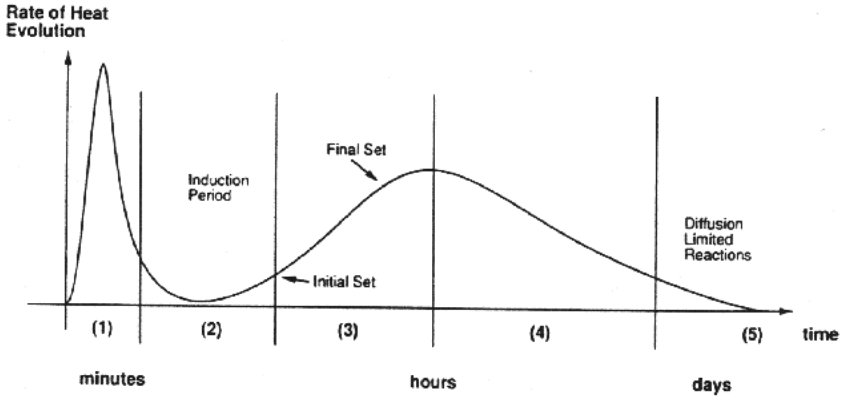

Figure 2. Stages in the hydration of cement.

(1) This initial exothermic peak indicates the rapid initial reaction (~15mins) during which hydrolysis of C_3S results in the release of Ca^{2+} and OH^- ions from the surface of C_3S grains. The hydration rate is governed by a topo-chemical mechanism. This hydrolysis slows down quickly but continues throughout the induction (or dormant) period.

(2) Indicates the induction period lasting several hours (hydration is almost halted). Dissolution of ions continues. The reason why hydration is inhibited here is unclear**.**

(3) Acceleratory period during which C-S-H and CH form via crystallization of ions when Ca^{2+} and OH^- ion concentrations super saturate. When the products crystallize, hydrolysis of C_3S proceeds again rapidly (nucleation and growth control).

The hydration products provide anchors on which more C-S-H can form, forming a coating, growing in thickness around the C_3S grains. Hence it becomes difficult for water molecules to reach the anhydrous C_3S and the production of hydration products slows down, as it takes longer for water to diffuse through the coating as observed by [19] who suggested that C- S-H clusters form by, "heterogeneous nucleation at the C_3S surface and then grow by accumulating C-S-H units."

(4) This leads to the period of deceleration (hrs-days) where the hydration is now under diffusion control.
(5) Diffusion control then continues steadily with a slow deposition of hydration products (C-S-H and CH) into the pore network, which is the space originally occupied by water.

2.2.2.1 Induction period theories

While there is general agreement on the framework of hydration, the fundamental mechanisms governing it 'aren't yet fully understood'. For example reasons for the C_3S induction period beginning and ending is subject to several theories including:

1. Initial reaction products forming a 'protective' over the C_3S particles, which when destroyed or more permeable indicates an end to the induction period. [20].
2. A nucleation and growth mechanism of C-S-H production controls the reaction rate in the induction and acceleratory periods. The induction period ending when growth begins.
3. SiO_2 poisoning of the CH nuclei causes the induction period. It ends when the level of super saturation is enough to overcome this and CH products crystallize.

There is not yet a agreed upon mechanism for what causes the induction period termination Young et al. [21] observed the end of the induction period to be linked to the onset of portlandite formation. This supports the nucleation and growth mechanism, with Ca^{2+} and OH^- concentrations rising until portlandite nucleation happens.

2.2.3 C_3A hydration

The hydration of pure C_3A involves a rapid formation of calcium aluminate hydrates

$$C_3A + 21H \rightarrow C_4AH_{13} + C_2AH_8 \qquad (2.2)$$

These hydrates aren't stable and quickly convert to cubic hydrogarnet C_3AH_6 [13].

$$C_4AH_{19} + C_2AH_8 \rightarrow 2C_3AH_6 + 9H \quad (2.3)$$

Where the phase C_4AH_{13} sometimes exists as C_4AH_{19} if there is water present in the interlayer between the hydrate coat and anhydrous grain.

C_2AH_8 has been observed in research papers as an intermediate hydrate by Jupe et al (1996) [22] and Christensen [23] observed C_4AH_{19} converting to C_3AH_6 in C_3A-water systems containing a low amount of gypsum (less than 10 wt%).

While I am looking at pure C_3A, in industry Calcium sulphates like gypsum are added to cement paste to prevent flash setting. Sulphate addition causes ettringite formation, which is known to form a coating around the anhydrous C3A, grains (similar to the C-S-H coating observed in C_3S hydration), thereby slowing the reaction.

However even with moderate gypsum content, the formation these Calcium Aluminate Hydrates (also called Afm phases) on C_3A grains has been observed at the very start of the reaction [24], followed by ettringite crystallization. Therefore these hydrates form regardless of the presence of gypsum as seen in by Pourchet et al. (2009) [25].

2.2.4 Hydration theories and mechanisms

The two opposing theories for the mechanism of cement hydration are the through-solution reaction mechanism and a solid-state dissolution theory. According to the through solution mechanism, the dissolution of anhydrous cement grains when mixed with water results in a saturated solution from which crystallization of hydrates transpires. These hydrates cover unreacted grains so that further reaction is controlled by diffusion of dissolved ions through the barrier. [6]

On the other hand, the solid-state theory suggests that the formation of an initial protective barrier formed from hydrates on the surface of the anhydrous grains prevents water getting through and the reaction is then controlled by the diffusion of water through this coating. [26].

2.3 Microstructural properties of cement phases

Cement hydration is dependent on the chemical composition, particle size distribution and W/C ratio.

2.3.1 Crystallite size effects

Polycrystalline materials such as cement mixtures are composed of microscopic crystallites and the crystallite size can be defined as the size of the "coherently scattering domains"[27] and can be calculated via XRPD analysis techniques as will be shown in chapter 3.

The size of the composite particle (and hence contained crystallites) greatly affects its rate of hydration. Hydration starts at the surface of a particle, so the finer the particles the greater the surface area (S.A) and hence the rate of hydration is increased [4], resulting in a more rapid development of compressive strength.

The effect of S.A on the hydration rate supports the fact that dissolution of the anhydrous grains governs the initial reaction with the nucleation sites of C-S-H on the surface thus higher surface areas would clearly result in a faster reaction.

Fineness is carefully controlled in industry; an increase in the fineness requires an equivalent increase in the amount of gypsum due to the increases amount of C_3A available for early hydration [28]. Particle size distribution is therefore critical for controlling the rate of cement setting and strength development. C_3S is the most abundant phase of OPC, and its particle size distribution directly affects the hydration kinetics and microstructural properties of cement pastes.

Most previous studies have focused on the overall effects of the S.A and particle size distribution on hydration kinetics, which is now well understood. However there's not yet a good understanding of the influence that particle size has on microstructural development during hydration with the only relating work by Kondo et al in 1971

showing that during hydration the size and the shape of initial C_3S grains remain unchanged [29].

2.3.2 Strain

The micro-lattice strain is due to the emerging contact forces between anhydrous crystallites and hydrates [30]. It is the formation of hydrates in the capillary pore space of cement-water systems that exert forces on one another and on the unreacted grains, causing strain build up.

Lattice strain is "a measure of the distribution of lattice constants arising from crystal imperfections" and describes the structural deviation of a crystal due to imperfections such as lattice dislocations, contact stresses and stacking faults [27].

Further sources of strain could be: thermal strain as a result of the significant liberation of heat during hydration [31] and shrinkage effects: The total volume of hydration products is smaller than the combined volume of the reacted cement and water – this is referred to as "chemical shrinkage" of the cement paste and is the main cause of the 'self-desiccation shrinkage' which is defined as the bulk shrinkage of cement paste in a closed isothermal system (i.e. without moisture exchange). This self-desiccation is a part of autogenous deformation in cement and also includes carbonation shrinkage due to reaction between CH and CO_2 in air [32]. Shrinkage during hydration can cause cracks in building materials. [33]The microstructural changes occurring in the lead up to the cracking hasn't been studied → so interrogating the strain of individual phases during hydration is beneficial to finding the evolution of microstructural change that could cause shrinkage

W-H plots are used to visualize the contributions of domain size and lattice microstrain discussed here to the peak broadening in diffraction patterns - see chapter 3.

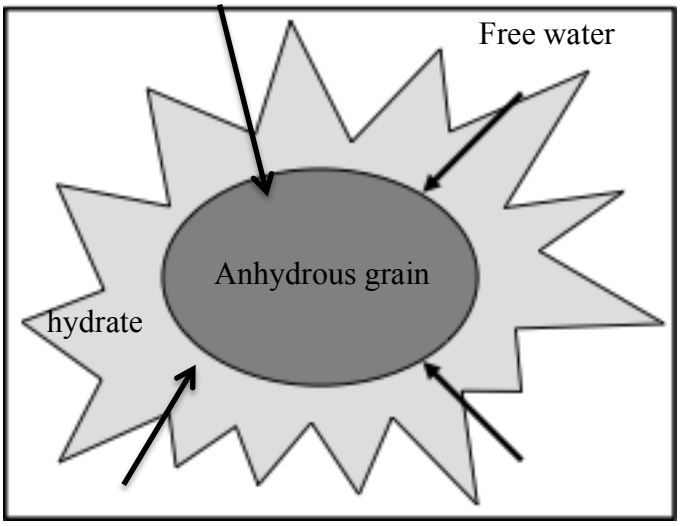

Figure 2.2: Schematic of the diffusion of free water through layer of hydrates (the black arrows indicate direction of flow. (modification of diagram from [34]).

3. Theoretical Background of experimental methods and analysis

3.1 Introduction

In-situ X-ray powder diffraction will be used to monitor the microstructural properties (crystallite size and lattice strain) during hydration of C_3S and C_3A. XRD is used extensively in the analysis of materials, both crystalline and non-crystalline (amorphous), to obtain information at the atomic scale. Interpretation of the diffraction patterns, resulting from the interference of X-rays scattered by atomic planes, provides structural information i.e. crystallite size, lattice strain and chemical composition of compounds to name a few [27]. XRD used on PC pastes can prove challenging due to overlapping or coinciding reflections from the 4 minerals [35]. Hence XRD of single phases will help eliminate this making it easier to spot emerging hydrate products.

XRD is commonly used to investigate cement systems and their hydration. [7]. Advancing XRD technologies and radiation strengths are allowing for more detailed data to be collected. The theory of XRD is reviewed in this section

3.2 Crystal Structure

Solids can divided into 3 groups; single crystal, polycrystalline and amorphous

Figure 3.1: Schematic of a single crystal, polycrystal and amorphous atomic positions [43]

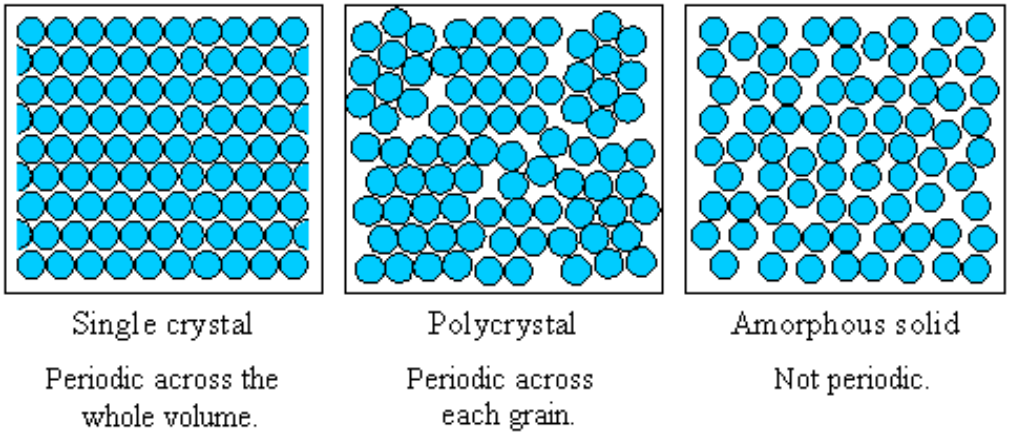

In crystals, atoms are arranged periodically in 3 dimensions and possess long-range order reaching distances greater than the interatomic spacings. For a single crystal the long-range order is present over the entirety of the specimen. Polycrystalline materials on the other hand are composed of lots grains (many small single-crystal regions) of different shapes and sizes, separated by boundaries with the grains on opposing sides of the "grain boundary" having different orientations with respect to each other [27].

Amorphous materials are "without definite form", exhibiting only a short-range order that extends to nearest neighbour atoms. A crystalline material will show sharp peaks representing x-rays diffracted from the lattice planes, whereas an amorphous material exhibits a broad peak due to it not possessing long-range order. Hence the amorphous hydration products e.g C-S-H cannot be directly identified via XRD but is indirectly indicated through time delays before emergence of crystalline hydration products CH in C_3S hydration or by the presence of a broad "hump" in the background intensity.

A unit cell represents the smallest repeating structural arrangement in a crystal lattice that can be stacked up to fill 3-D space, with three fundamental vectors mapping it's 3-D structure in space relative to the cell origin, given by the lattice vector:[27]

$$R_n = n_1 a_1 + n_2 a_2 + n_3 a_3 \quad (3.1)$$

The side lengths and interaxial angles make up the lattice parameters of a unit cell and these can be used for identification of a structure. Miller indices identify the crystal planes in a lattice, which are parallel equidistant planes making intercepts a_1/h, a_2/k and a_3/l along the 3 crystal axes. [36].

For a cubic unit cell;

$$d = \frac{a}{\sqrt{h^2+k^2+l^2}} \quad (3.2)$$

where a is the cell parameter, (h,k,l) are the miller indices and d is the interplanar spacing. The spacing and orientation of the crystal planes defined by (hkl) are used in Braggs law.

3.3 X-Ray Diffraction

3.3.1 x-rays

X-rays have energies ranging from 200eV to 1Mev, corresponding to wavelengths between 10nm and 1pm, which is of the same order of magnitude as the interatomic spacings of most crystals - usually about 0.2nm (2 Å).[27] X-rays are formed when electrons produced by heating a cathode (e.g tungsten), are accelerated over a potential difference towards the target anode, and the energy lost on impact with the anode is released as x-rays.

The spectrum of x-rays released consist of a spectrum characteristic of the target anode material - produced when an electron with sufficient energy to eject an inner shell electron is incident on the target atom, leaving a hole in the atom that is quickly filled by an outer shell electron causing the release of an x-ray photon with energy equivalent to the difference between the energy levels. This characteristic spectrum is superimposed on a continuous background spectrum due to electrons coming to rest in the target after a series of collisions.

Figure 3.3: Shows the characteristic spectrum of copper sourced X-Rays superimposed on the bremsstrahlung

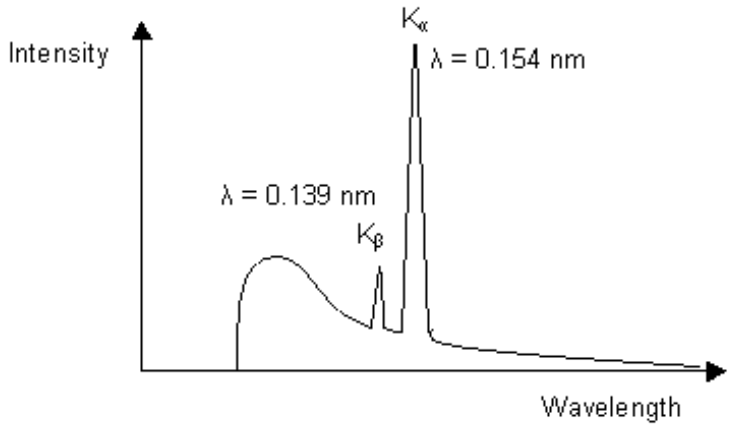

The inner electron shell is called the K shell, and is followed by the L shell and them M shell working outwards from the nucleus. When an electron from the L shell fills the hole in the inner K shell, a Kα x-ray is produced. A Kβ X-ray is released when the 'hole' is filled by an electron from the M shell.

Figure 3.4: Schematic of electron shells- here we see the production of a kβ x-ray as the hole in the k shell is filled by an electron from the m shell. (Source http://prism.mit.edu/xray)

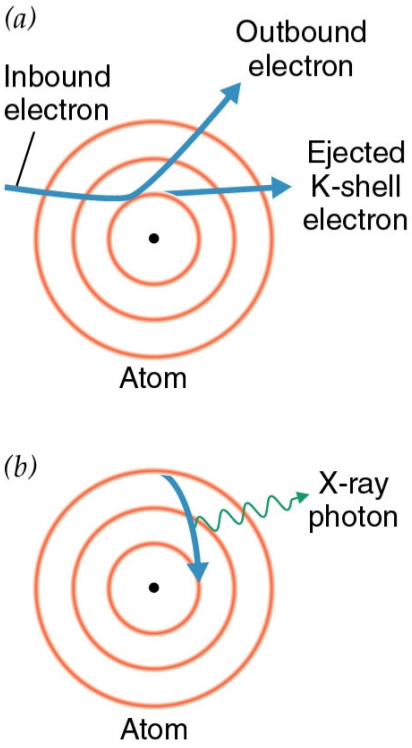

Kβ x-rays have a higher energy than Kα but Kα transitions are 10 times more likely due to being closest to the hole within the k-shell. Now the L-shell consists of 3 subshells L_1, L_2 and L_3. A transitioning electron coming from L_3 to fill the hole in K emits a $K\alpha_1$ x-ray and one from L_2 to k emits a $K\alpha_2$. A Nickel filter with an absorption edge midway between the Kβ and Kα line is used in the diffractometer to eliminate (heavily reduce) the Kβ peak .$K\alpha_1$ and $K\alpha_2$ peaks can be seen, and are easily distinguished at higher 2θ angles where they are better resolved. [27].

3.3.2 Bragg and Laue descriptions

Max von Laue discovered that crystalline substances can act as 3D diffraction gratings for x-rays possessing wavelengths of the same order of magnitude as the interplanar spacing of crystal structures in 1912 [37].

XRD involves directing an incident wave into a material and recording the outgoing diffracted wave direction and intensity using a detector. Scattered waves emitted from atoms of different type and position, interfere constructively or destructively, along different directions. The crystal structure of a material is related to the directions of constructively interfering waves, which form the "diffraction pattern" via Braggs Law [38].

$$2dsin\theta = n\lambda \tag{3.3}$$

where λ is the X-ray wavelength, diffraction angle θ ,lattice spacing ,d of the crystal and n is the order of diffraction [38]

Figure 3.5: Bragg representation o the diffraction of X-rays from lattice planes (adapted fromhttp://en.wikipedia.org/wiki/File:BraggPlaneDiffraction.svg)

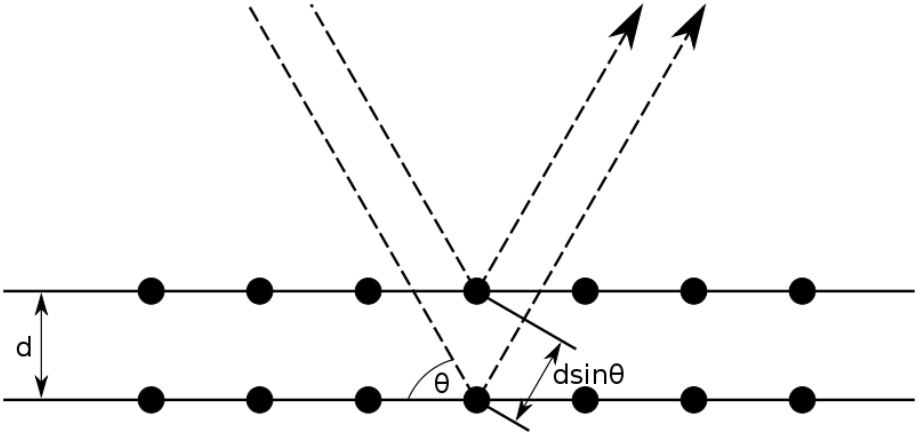

Braggs law [38] relates the wavelength of the incident x-ray beam to the angle of diffraction and interplanar plane spacing in the crystal sample.

The diffraction pattern represents a spectrum of real space periodicities in the crystal. Due to the random orientations of crystals in a powder, all possible diffraction directions can be obtained by scanning the sample over a 2θ range. Each mineral has a diffraction

pattern “fingerprint” and so converting the diffraction peaks to d-spacings and comparing to a standard reference file allows identification of said mineral.[38]

3.3.2.1 The reciprocal space connection

To grasp the physical concept of diffraction, reciprocal space is mentioned. Reciprocal space maps onto real space through a fourier transformation, and the wave signals reflected from an atomic plane are the output of a fourier transform of the crystal lattice. Hence “a point in the reflected space comes from a 3D object in real space”[36]. The reciprocal lattice is a mathematical concept that provides an illustration of the translational symmetry of crystals. It is derived from the real lattice as a set of vectors ,G_n, perpendicular to the real lattice planes (h,k,l) and with lengths $1/d_{hkl}$.
Following on from the real space lattice vector given in (3.1), the reciprocal lattice vectors are defined as

$$G_n = ha_1^* + ka_2^* + la_3^* \quad (3.4)$$

where the reciprocal space vectors (a_1^*, a_2^*, a_3^*) can be derived from the real lattice vector by

$$a_1^* = 2\pi \frac{a_2 \times a_3}{a_1.a_2 \times a_3} \quad (3.5); \quad a_2^* = 2\pi \frac{a_3 \times a_1}{a_1.a_2 \times a_3} \quad (3.6); \quad a_3^* = 2\pi \frac{a_1 \times a_2}{a_1.a_2 \times a_3} \quad (3.7)$$

The Ewald sphere is a visualization in reciprocal space of the conditions for diffraction to occur, by superimposing the scattering triangle onto the reciprocal lattice. The observed Bragg peaks will be from those lattice points that lie on the circumference of the sphere.
Ewald sphere with triangle

Figure 3.4: Ewald sphere with scattering triangle

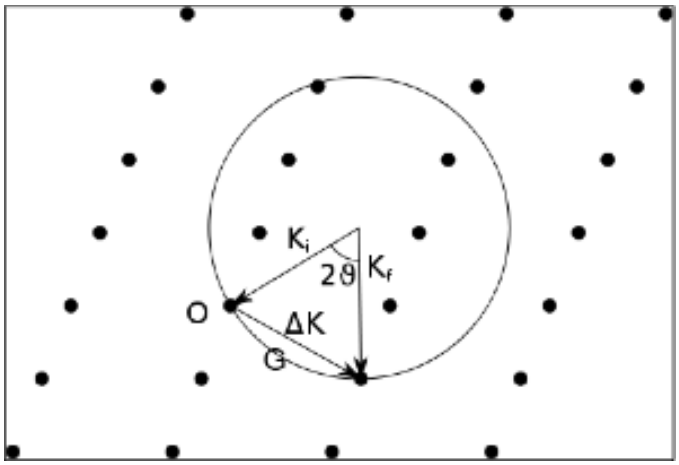

The Laue condition for constructive interference between the incident and scattered beam, and consequently diffraction to occur is Q=Gn [36].

Where Q is the scattering vector:

$$Q = k_f - k_i \tag{3.8}$$

(scattered –incident wavevector; $k = \frac{2\pi}{\lambda}$) and G_n is a reciprocal lattice vector as defined in equation 3.4 From this we can obtain the Bragg result;

$$Q = \frac{4\pi sin\theta}{\lambda} = G_n = \frac{2\pi}{d_{hkl}} \tag{3.9}$$

$$\longrightarrow \lambda = 2dsin\theta$$

3.3.3 Powder Diffraction

Measuring a material in powder form results in the random orientation of many tiny crystals with respect to the x-ray beam so there will always be several crystals in the correct orientation for diffraction according to Braggs law. At any one time there will be many planes each reflecting the beam along different directions so the powder sample is equivalent to a single crystal being rotated through all angles. It creates a 1D projection of the 3D reciprocal space which can cause problems due to overlapping reflections [36] Nonetheless, a unique pattern is produced for a given material that can be identified by comparison with a database. Bragg Brentano configuration is often used for powder diffraction.

3.3.3.1 Advantages and limitations of XRPD

XRPD inherently averages over many grains and as such is preferred over the TEM technique for the analysis of grain size and strain in microcrystalline materials.
For XRPD, the material to be analyzed must be ground to an appropriate fineness so as to minimize primary extinction of the most intense peaks, but not too strongly otherwise it may lose some crystallinity [39]. Also there must be enough crystals to fulfill the diffraction condition for each lattice plane. Amorphous phases only serve to increase the background intensity therefore XRPD doesn't identify them directly.

3.3.4 The XRP Diffractometer geometry

Generally XRPD uses a "Bragg-Brentano" geometry, which allows for illumination of a reasonable area of the specimen surface.

Figure 3.5 Bragg Brentano Beam schematic (source: [40])

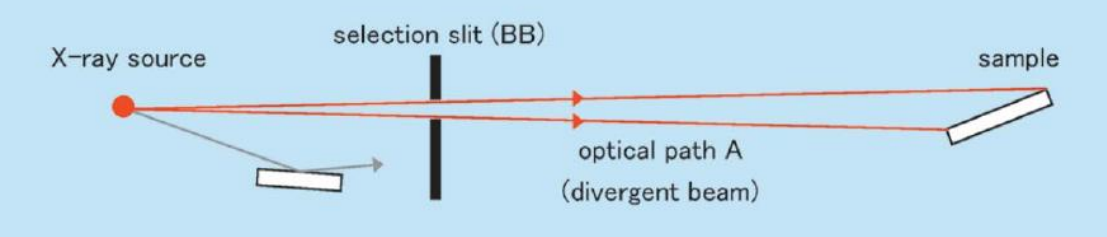

Diffractometer's all have an x-ray source, detector and sample located on the circumference of the 'focusing circle'. Another circle known as the diffractometer or goniometer circle is centered on the sample and has a fixed radius.

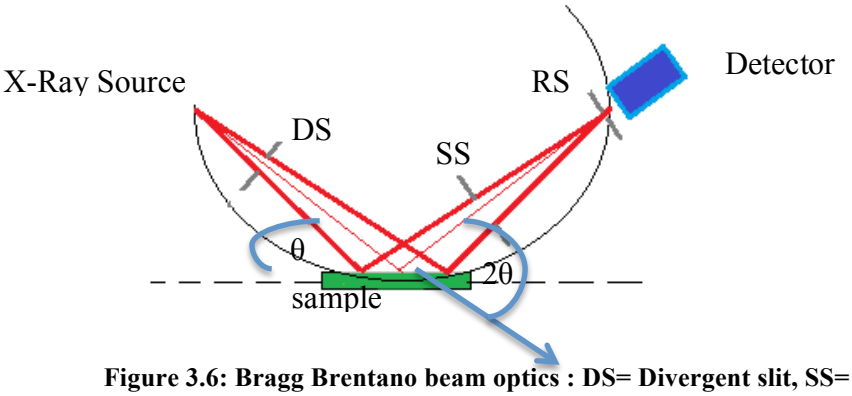

Figure 3.6: Bragg Brentano beam optics : DS= Divergent slit, SS= Scattering slit, RS= receiving slit

In figure 3.6, θ, the Bragg angle, is the angle between the source and sample. And 2θ is the angle between the projection of the x-ray source and the detector. Hence θ-2θ scans. In this arrangement the specimen lies flat with the face of the sample forming a tangent to the focusing circle. This results in some broadening of the diffracted beam and can cause the Bragg peak position to shift slightly to smaller angles. [41]

After emerging from the x-ray source, the beam passes through soller slits, which are boxes with many metal sheets parallel to the plane of diffraction. They limit horizontal divergence of the beam (typically 5°) and the resulting low-theta contribution to peaks. The length limiting slits simply reduces the horizontal footprint of beam on sample
The divergence slit then chooses the width of the incident beam on the sample. On the receiving side, after the beam has been diffracted by the sample, it travels through anti-scatter slits to reduce background noise, improving peak-to-background ratios and helping the detector to receive x-rays only scattered from the specimen. The beam is then converged at the receiving slit, towards the detector. The integrated intensity (peak area) is independent of slit width and is used for phase quantification later on. A scintillation counter acts as the detector.

3.4 Data Analysis techniques

3.4.1 Average Size and Lattice-strain determination; W-H analysis

Following the XRPD measurements of C_3S and C_3A, the resulting diffraction patterns will be carefully analyzed using the well-known technique of WH analysis. This section provides the theoretical details of the technique.

Braggs law assumes that the diffraction takes place under ideal conditions, i.e a perfect crystal and a completely monochromatic the x-ray beam, resulting in extremely thin peaks, however in the real world peaks obviously have a measureable width.
The broadening of diffraction peaks arises primarily due to three factors:

1. Instrumental effects: the incident beam divergence and source width. Unresolved Kα1, Kα2 peaks (luckily the PDXL software deconvolutes these on automatically and supplies the FWHM of the Kα1 peak)

2. Crystallite size: Peaks are broadened due to small crystallite sizes, enabling peak broadening analysis to be used to determine crystallite sizes in the range of 100-500nm [27]. Supposedly Crystals consist of domains that are marginally disoriented with respect to each other, hence some domains may cause diffraction just before the Bragg angle while others are in a position to diffract just after, thereby broadening the peak.
3. Lattice strain:

This broadening of diffraction peaks causes the peak height to be reduced, while the FWHM increases thereby maintaining a constant integrated intensity. The Bragg angle stays constant. The three factors contributing to peak broadening can be separated to find the average lattice strain and crystallite size values of samples.

Deconvolution of the peak broadening contributions

The first step toward determination of crystallite size and strain is to find the diffraction breadth that is due to small crystallite size only. The broadening is taken as the width of the peak at half the maximum intensity of the peak – FWHM.

Let β= observed peak width (FWHM)

$\beta_{observed} = \beta_{instrumental} + \beta_{strain+particle\ size}$

$$\beta_o = \beta_i + \beta_r \quad (3.10)$$

The instrumental contribution to peak width is determined by calculating a FWHM correction curve by measuring the diffraction pattern of a well annealed powder (standard Silicon powder was used) sample under the same BB settings.

Figure 3.6: FWHM curve of standard Si for instrumental broadening determination

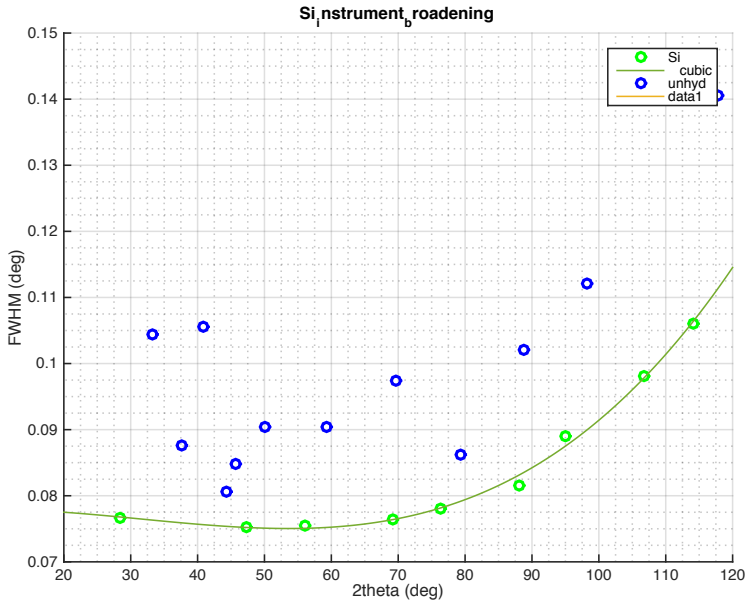

Re-arranging equation 3.10, the broadening due to size and strain is then;

$$\beta_r = \beta_o - \beta_i \tag{3.11}$$

Equation (3.10) is the lorentzian peak profile expression. However a Gaussian profile is approximated and so the Gaussian expression for the correction is used instead;

$$\beta_r^2 = \beta_o^2 - \beta_i^2 \tag{3.12}$$

The Scherrer formula derived in 1918 [42] relates the mean crystallite size, D, to the peak broadening β_r (the FWHM after instrumental broadening correction) ignoring strain effects via

$$D = \frac{k\lambda}{\beta_{size}\cos\theta} \tag{3.13}$$

It is used for grain sizes in the range 2nm to 300nm and is based on the assumption of Gaussian peak profiles. K is a dimensionless constant, whose value lies between 0.89 and 1.39 depending on crystallite size and shape. β is the angular width in terms of 2θ measured in degrees but must be converted to radians in the equation.
The Scherrer equation shows that D and β are related reciprocally – the greater the broadening, the smaller the crystallite size will be i.e. interference becomes more precise with increasing number of scattering planes.

Lattice strain also causes peak broadening, with deformations resulting in changes to the d-spacings, which alters the 2θ positions of diffracted x-rays. For example consider crystallites compressed equally, resulting in isotropic strain and reducing the d-spacing;

d→ d-δd. Then for Braggs law to hold, the peak position needs to increase from 2θ to 2(θ+δθ)

$$\lambda = 2d \sin\theta$$

$$\lambda = 2(d - \delta d) \sin(\theta + \delta\theta)$$

Hence in this case the peak position is shifted to a higher Bragg angle.
Uniform strain like this where all crystallites are strained homogeneously, causes a shift in the peak position only, with no peak broadening effect: simplest strain type and called "uniform dilatation". The d-spacings increase slightly under tensile stress, which has the alternate effect of shifting the Bragg angle to lower values [38].

However in a polycrystalline sample, strains are generally distributed unevenly with some particles experiencing compression and others tension. This non-uniform strain causes the grains to be pulled in different directions causing a non-uniform change in the d-spacing; d-spacing decreases on one side, remaining the same in a defined middle position and increases on the top planes. Thereby the net effect of this non-uniform strain is to broaden the resulting diffraction peak. Peaks located at higher Bragg angles exhibit more broadening than those at lower angles. Non-uniform strain can be caused by point defects (vacancies, site disorder), plastic deformation and poor crystallinity.

Stokes and Wilson (1944) [44] empirically found the broadening from crystallite strain to be given by:

$$\beta_{strain} = 4\varepsilon tan\theta \quad (3.14)$$

Where ε is the strain and θ the Bragg diffraction angle and the strain induced broadening increases with Bragg angle.

3.4.1.1 WH Analysis

The size and strain broadening contribution vary differently as a function of 2θ and hence can be separated. Williamson and Hall then proposed a method for deconvolution of the size and strain broadening to the diffraction peak [45]

Having subtracted the instrumental broadening effect:

$$\beta_r = \beta_{particle} + \beta_{strain} \quad (3.15)$$

Substituting in the relevant equations

$$\beta_r = \frac{k\lambda}{D\cos\theta} + \varepsilon \tan\theta \quad (3.16)$$

And multiplying by cosθ,

$$\beta_r \cos\theta = \frac{k\lambda}{D} + 4\varepsilon \sin\theta \quad (3.17)$$

This equation has the form of a straight line and so plotting $\beta_r \cos\theta$ against $\sin\theta$ forms a Williamson-hall plot from which one can estimate both mean crystallite size and lattice-strain from the gradient and y-intercept of the linear best fit line to the data points.

$$\varepsilon = \frac{gradient}{4} \quad (3.18)$$

$$D = \frac{k\lambda}{y-intercept} \quad (3.19)$$

The Williamson hall method is not the most accurate determination of these quantities but it allows for relative trends to be attained

3.5 Qualitative and Quantitative phase determination

The phases are identified by comparison of the diffraction pattern, d-spacings and relative peak intensities with the Crystallography Open Database (COD). This can be done using the autosearch function on the PDXL software. However the autosearch proved erroneous and it was combined with manual fitting – selecting phases form literature and checking whether it was a match to the measured data etc.

The growth and decline of phase concentrations is monitored by plotting graphs of the integrated intensity of a peak representative of a particular phase against time

4. Experiment Methodology

4.1 The Smartlab Rigaku Diffractometer and software

X-ray diffraction was performed using the Smartlab Rigaku x-ray diffractometer with Cu-Kα radiation of wavelength λ=1.5406 Å. The controlling software, "Smartlab Guidance", enables the user to select the measurement package – in this case "@General Bragg Brentano focusing" for powders is used - and guides the user through optical alignment, sample alignment, slit and scan settings. Fast data collection is enabled by a 9 kW rotating anode source, which produces a high flux of X-ray intensity.

Rigaku Integrated Powder Diffraction Software (PDXL) version 2.2 is used to display the obtained diffraction patterns. It automatically finds accurate values for the intensity, FWHM and 2θ position of peaks. PDXL contains many useful functions for data analysis however only the "Autosearch" and RIR quantification functions were unlocked. The autosearch function is an algorithim used to compare the degree of coincidence between the experimentally measured data and data base patterns (COD used). It searches for major and minor phases until all the peak intensities are matched. However often it

identified a phases that the sample clearly was not and so manual search and matching of the experimental data to database patterns had to be done by finding from literature expected hydration phases and checking if it matched the measured data.

Figure 4.1: Smartlab Rigaku Diffractometer

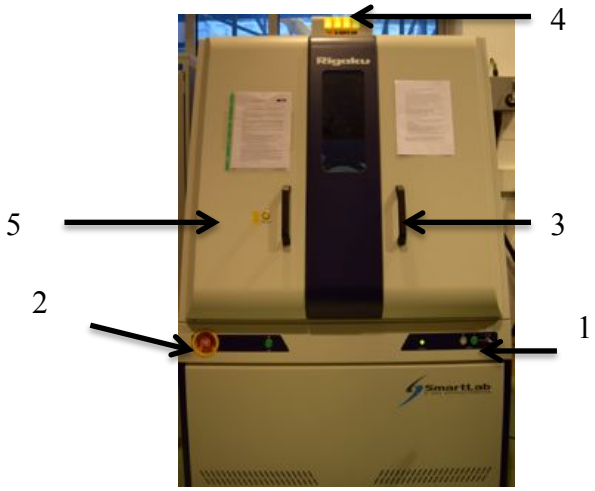

Table 4.1: Indicates the name of parts in Fig 1

1. Main panel	Panel used to start and stop
2. Operating panel	Panel used to turn the internal
3. Door	This door is opened to change samples and
4. X-ray warning	Lights when x-rays are
5. Door-lock button	Lock/Unlock the door.

To begin with time was spent determining the optimum machine settings to measure the samples with throughout the investigation and checking that the machine could reliably reproduce accurate 2θ measurements.
After considering several options, a Bragg Brentano optical configuration (see figure 3.7) was chosen.

A θ-2θ scan mode is employed where both the x-ray source and detector move in synchronized motion about the fixed sample stage. The machine was operated at the maximum load power of 9Kw in order to attain maximum possible intensity to enhance the counting statistics.

A nickel filter is inserted in the diffracted beam path between the sample and detector, to eliminate Kβ wavelengths. $K\alpha_2$ is not removed and we see that peaks split up at higher 2θ angles. This does not pose a problem because the PDXL software automatically finds the 2θ and FWHM of the $k\alpha_1$ peak.

Table 4.2: The BB scan setting used throughout the investigation

Incident Parallel Slit	Incident slit	Length limiting slit	Receiving slit 1	Receiving slit 2	Receiving optical device	Receiving parallel slit	attenuator
Soller slit 5 deg	2/3 deg	10mm	2/3 deg	0.3mm	PSA_Open	Soller slit 5 deg	open

4.2 Sample prep:

The samples were prepared by grinding in a pestle until they had the consistency of flour. If not ground long enough, it was observed that the powder easily fell out of the trench. For the C_3A sample that came in a solid block form, clean pliers were used to break off fragments that were then ground up in the pestle.

Figure 4.2: Pestle used to grind sample

The powdered sample is then carefully deposited into a rectangular glass sample holder of trench depth 0.2mm using a spatula and smoothed level in the trench using a microscope slide. Note: Protective gloves and glasses were worn, and all apparatus thoroughly cleaned and dried using ethanol prier to preparation.

The mass of sample within the trench is then measured using scientific scales so that the sample phase can be hydrated with 0.5 W/C-ratio using a biological 20-200micro-litre Finn pipette.

Pritt-stick glue is applied around the sample trench and commercial cling film pulled taut to cover the sample immediately following hydration (likewise when the unhydrated scan is done) – this is done to help minimize irreversible hydration/carbonation of the sample

due to exposure to the atmosphere. The use of clingfilm served to only very slightly reduce the overall intensity, peak positions were unaffected.

To follow the microstructural changes and phase evolution, measurements were taken at regular time intervals: The following schedule of measurements was stuck to as far as possible. (Note the machine was turned off for 3 weeks in January and had many other users which halted measurements)

Time scale of measurements to undertake for the C_3S and C_3A samples:

unhydrated, 1h, 2h, 3h, 6h, 12h, 24h/1d, 3d, 5d, 7d, 10d, 14d, 18d,

(h=hour, d=day).

Scan lengths were adjusted according to the length of time passed:

Unhydrated sample: 30min + 1hr scan

The measurements once the sample has been hydrated were:

Up to 24h: 30min scan; to allow quick collection as this is where reaction is fastest.
1d-7d: 30min scan + 1hour scan;
beyond 7d: 30min scan + 2hour scan.

However in the end as rietveld refinement was not performed these long measurements were unnecessary but did however help when identifying phases with accuracy.

In between measurements the samples were kept in air tight plastic bags within airtight plastic boxes to provide protection from the atmosphere.

Samples were scanned over a range of 5° to 125°, with a 0.01° step widths and a scan speed of 4° per minute (for 30min scan), 2° per min for the 1hr scan and 1° per minute for the 2 hour scan. The temperature is assumed to be kept constant within the chamber ~Room Temperature (25°).

These measurement settings provided good counting statistics however due to the length of each scan (30 mins to 2 hours at later stages), the scan does not exactly represent the phase hydration time accurately.

Fig 4.3; Shows the sample held in the Height reference sample plate in the Smartlab diffractometer.

The sample is inserted into the height reference sample holder as shown in fig 4.3 and is fixed in place by clips. No sample height alignment is required as it is at the axis reference height.

Optical alignment is carried out before each new measurement. It finds the offset in 2θ and ω and corrects (zero's) them.

An attempt at hydrating the sample via a humid environment as opposed to direct hydration was done by placing a water bath in close vicinity to the sample in an enclosed environment using cling film. It results in much slower hydration rate and so was not employed further.

Throughout the investigation measurements of the Si reference sample were taken regularly to identify trends in any peak shift occurring and check that the peaks are correctly agreeing with database values and are reproducible.

See appendix 3 for a discussion and calculation of the uncertainties involved in taking measurements using the Smartlab diffractometer

5. Results and discussions

5.1 C3A

The peak positions and FWHM's obtained by PDXL are used to calculate the average crystallite size and lattice-strain, while the integrated peak intensities are used to see the rate of reactions and growth/decline of a phase.

5.1.1 WH results

The WH plots were plotted in excel by selecting a range of peaks across the diffractogram range 5-125° that were present during the whole 16day period. These peaks were manually tracked and then the W-H plots built. The y-intercept and gradient of the best fit line was found accurately using the LINEST function. The majority of plots resulted in negative linear fits indicating non-physical negative strains. Therefore it is considered to be a null result without strain[46]. Calculating the associated errors, we see that a horizontal fit (to indicate zero strain) is within the experimental uncertainty of the data points The full set of plots can be seen in appendix 1 along with explanation of errors and error propagation in appendix 2.

Graph 5.3 W-H plot at 1hr hydration of C3A with extrapolated horizontal fit shown to be within error bars.

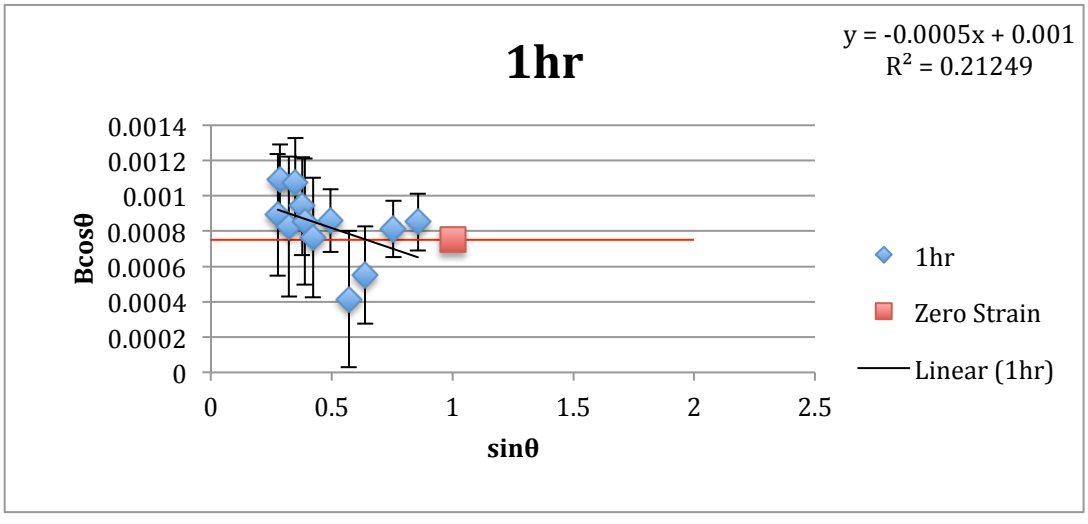

However the average crystallite size obtained from the W-H plots correlates with that obtained when strain is not taken into account by using the Scherrer formula (see graph 5.1). The Scherrer formula is used to calculate the average crystallite size of the same range of peaks as used for the W-H analysis.

Table 5.1: values obtained for the average crystallite size and lattice strain of the C_3A at designated times up to 16 days via the W-H graphical method and when eliminating strain via the Scherrer formula

	Time (hrs)	W-H Average crystallite size ($x10^{-7}$m)	W-H Average lattice strain $x10^{-4}$	Average crystallite size from Scherrer only ($x10^{-7}$m)	Crystallite size from horizontal fit ($x10^{-7}$m)
unhyd	0.1	1.51	-0.911	1.98	1.931
1hr	1	1.38	-1.16	1.87	1.931
2hr	2	1.06	-2.2	1.78	1.6091
3hr	3	1.91	0.341	2.07	1.788
6hr	6	1.28	-0.616	1.55	1.448
12hr	12	2.53	1.2	2.05	1.45
20.5hr	20.5	2.32	0.342	3.27	1.48
3days	72	4.49	2.54	4.04	1.33
5days	120	2.16	1.54	1.96	1.29
7days	168	0.781	-3.41	1.47	1.43
10days	240	1.19	-0.971	1.99	1.46
16 day	384	0.993	-2.96	2.20	1.61

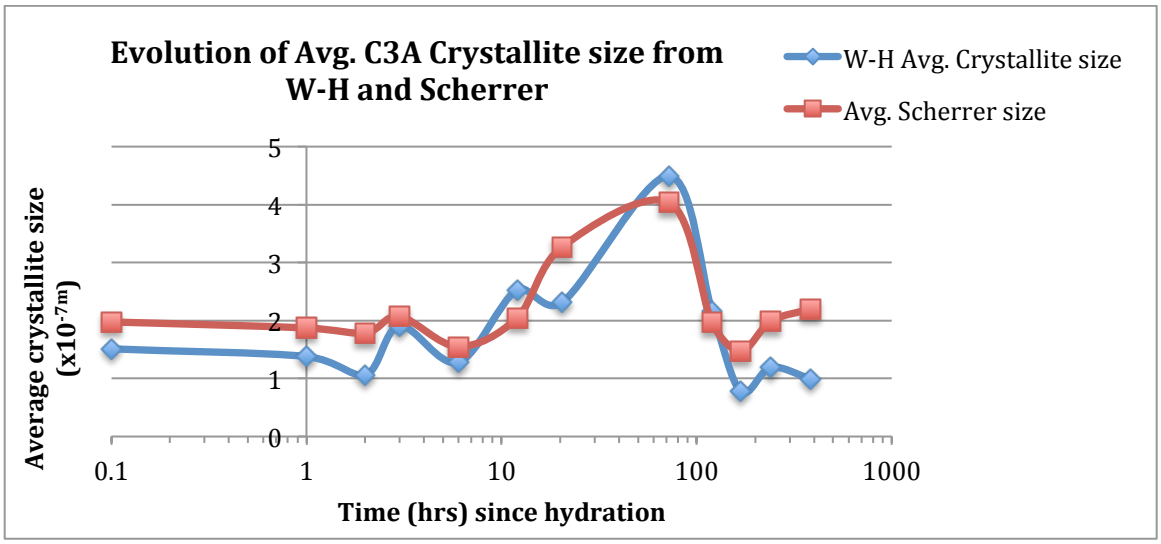

Graph 5.1: comparing the evolution of crystallite size when strain is considered (W-H) and when neglected i.e. zero strain using Scherrer. Use of a log scale for time.

Interestingly the average crystallite size obtained for both methods follows the same projection with time – both show the crystallite to decrease in size initially before reaching a maximum size at 3days and then decreasing to a minimum value at 7days and rising slightly to what appears to be a steady size. The final size is smaller than the original size for W-H, and larger by a little for the Scherrer.

Graph 5.2: Shows the evolution of crystallite size calculated via the scherrer formula using only individual peaks that represent C3A (log scale for time)

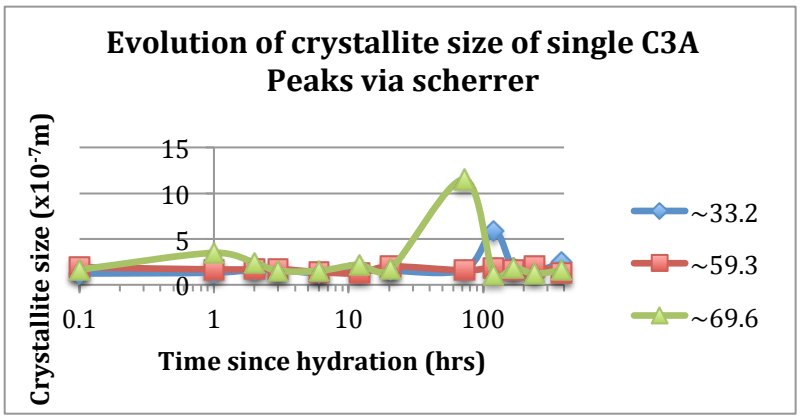

While the peak at ~59.3° stays steady, the others shows a sharp rise in crystallite size at 3days and 5days for the ~69.6° and ~33.2° peaks respectively.

5.1.2 Phase identification

The diffraction patterns obtained from the diffractometer are displayed on the PDXL software. Savitzky-Golay smoothing and background intensity subtraction is done before matching to the database. The unhydrated diffraction pattern was identified as calcium cyclo-hexaluminate ; $Ca_9(Al_6O_{18})$,which is C_3A (same crystal structure as $Ca_3Al_2O_6$)

The first diffraction pattern obtained after 1hrs hydration shows a noticeable decrease in peak intensity of the C_3A indicated it's high reactivity with water

Diffractogram 5.1: unhydrated and 1 hr diffraction patterns

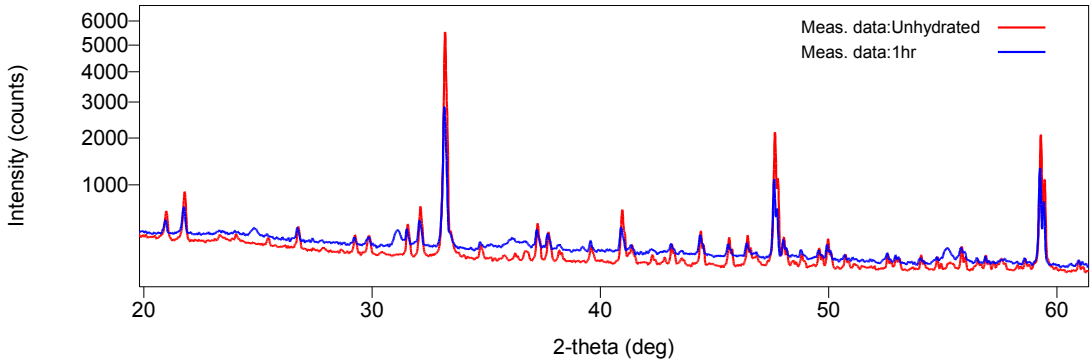

On removal of the background intensity, there is a clear hump revealed in the range 15-20° and one around 7°. These may correspond to an amorphous phase. They are also present in the unhydrated scan so exposure of sample to atmosphere on preparation (grinding did take 15 minutes) and inadequate sample storage has perhaps lead to some water attack.

Diffractogram 5.5: Background intensity humps indicate possible amorphous phase present

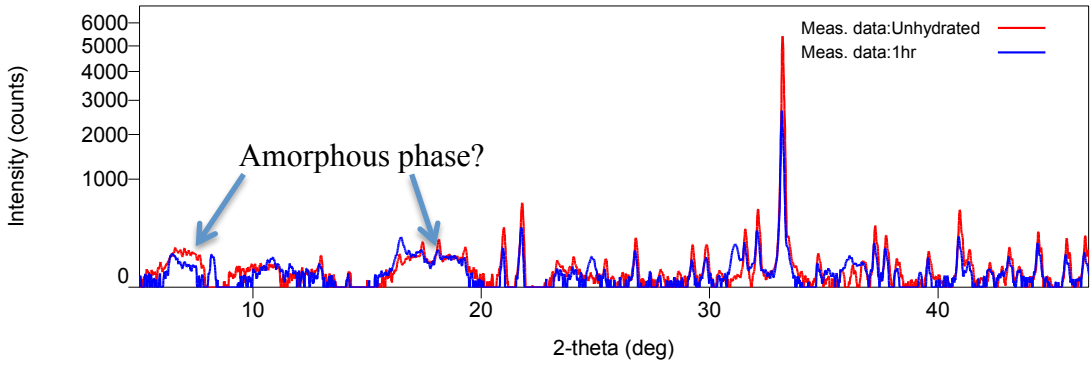

Hydrogarnet is matched to the peak at 44.39° and a trace amount of carbonated calcium hemicarboaluminate is picked up at 52.59° (indicates carbonation of sample) at 1hr.

This hydrogarnet peak only increases noticeably in intensity from 2hrs, at 2hrs other hydrogarnet peaks begin to emerge at 17.3°, 26.4°,28.4°,39.2°, 53.5° and 54.6°.

Diffractogram 5.6: continued increase in intensity of hydrogarnet and decline of original C_3A

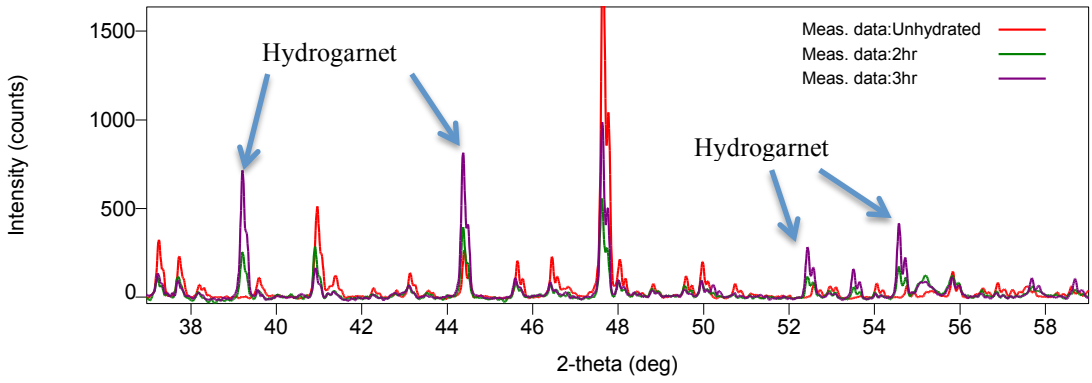

Hydrogarnet peak growth is significant at 3hrs (in fact peaks have doubled in intensity within the hour). All hydrogarnet peaks emerge mostly from 2hrs except the 44.39° peak which appears at 1hr , appearing to grow on top of a peak around present in the unhydrated sample.)

Diffractogram 5.7: Hydrogarnet peaks (in pink here) reach a maximum intensity at 12hrs, at which point the C_3A (Blue) is also maximally depleted

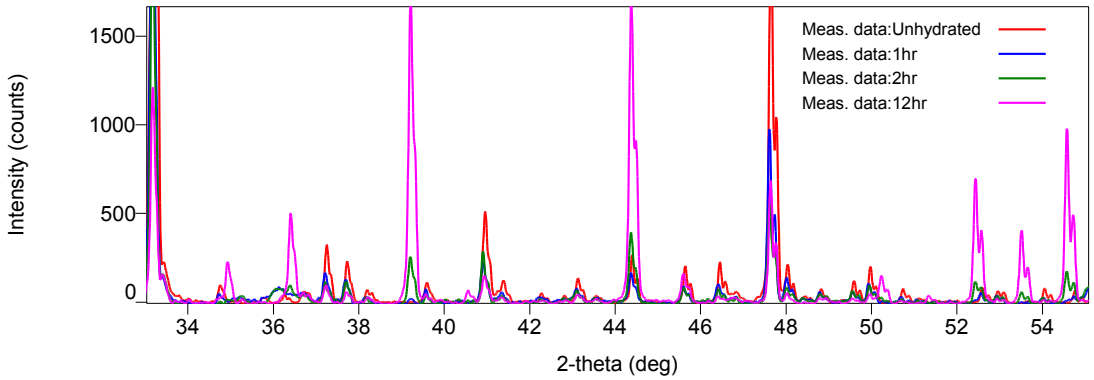

Diffractogram 5.8: At 16days most of the original C_3A peaks are more or less completely depleted except for the very strong 33.2° peak which remains present throughout;

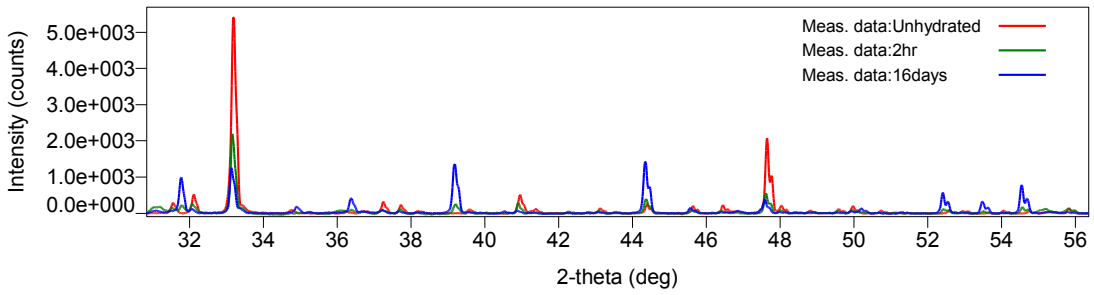

Diffractogram 5.9: the suggested 'amorphous' hump remains

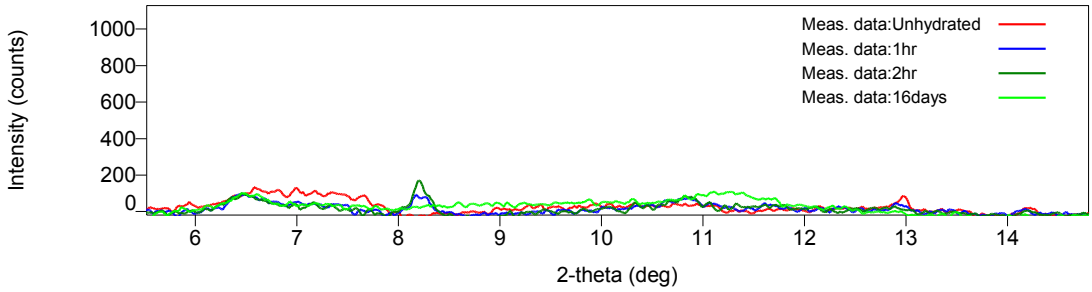

5.1.3 Rate of peak growth and decline

Plotting the integrated intensity against time, gives an indication of the rate of reaction as well as phase developments in the hydrating system and the quantities of constituent phases remaining and emerging.

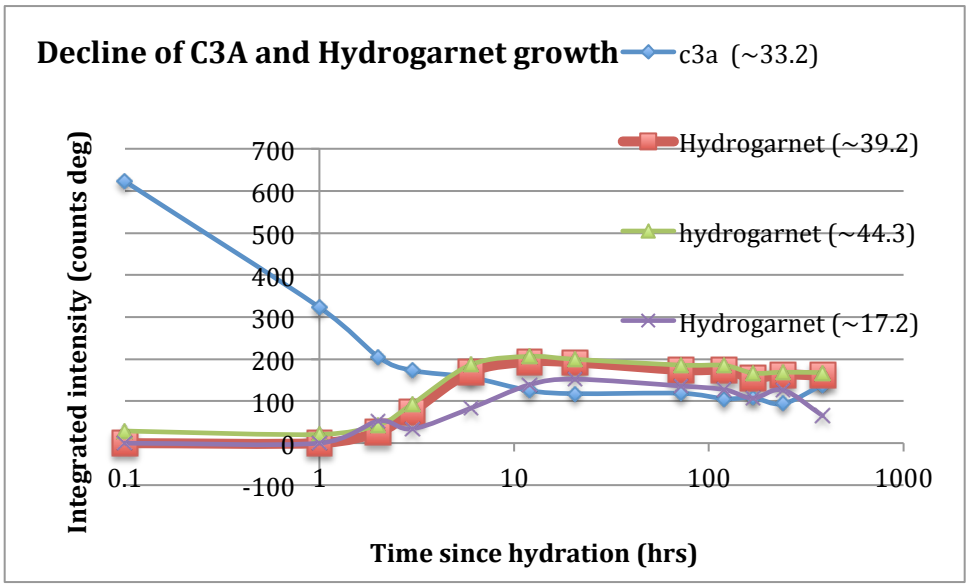

Graph 5.3: shows the decrease in concentration of the major (highest intensity) C_3A peak located at 33.2°. This has a rapid decline in the first few hours and begins to reach a steady level at 3hours. Immediate growth of the hydrogarnet hydrate product is seen from 1hr with the peak at 44.3°. The hydrogarnet reactions show rapid growth around 6hours and reach a maximum at ~12hours where they collectively level off having reached a steady state. The rapid growth phase of the hydrogarnet (between 3-12hours), occurs ~

3hours after the rapid C_3A decline. This indicates that following the quick dissolution of the C_3A in the first 3hours since hydration, there is a dormant period for a few hours before hydrogarnet crystallizes out in mass. i.e supports the theory of nucleation and growth.

The steady state intensity begins to slowly decline (decelaratory phase), probably due to the depletion of C_3A or less S.A of the C_3A grains being available for reaction due to more of C_3A surface touching the crystalline hydrates – i.e the reaction rate is now diffusion controlled

5.2 C_3S results

5.2.1 WH

C_3S on the other hand gives realistic physical values for the average crystallite size and lattice strains from the W-H plots.

Table 5.2: displaying the average C_3S crystallite size and lattice strain values obtained via the WH method and the size with the Scherrer formula

Measurement	Time (hrs)	W-H Average crystallite size ($x10^{-7}m$)	W-H Average lattice strain ($x10^{-4}m$)	Scherrer Average crystallite size ($x10^{-7}m$)
unhydrated	0	1.46	5.71	1.04
1hr	1	1.55	7.71	0.788
2hr	2	1.92	8.53	0.759
3hr	3	1.01	25.2	0.723
6hr	6	2.79	10.7	0.777
12hr	12	0.878	2.35	0.807
1day	24	1.45	5.82	0.991
2days	48	1.29	6.53	0.793
3days	72	1.07	3.86	0.843
7days	168	1.00	5.82	0.679
9days	216	1.30	6.82	0.829
11days	264	2.95	8.74	1.45

The average crystallite size of the C_3S decreases initially up to 3hrs and this correlates with an increase in the average lattice strain which reaches a maximum at 3hrs; this could correspond to the rapid dissolution of the C_3S resulting in increased ion concentrations

and the formation of crystalline hydrates emerging into the pore network of the system, producing contact forces on the unhydrated C_3S and therefore increasing strain. At 6hrs C_3S shows a sudden increase in size along with a decrease in strain.

However after 6hrs the strain appears to be almost proportional to the crystallite size – increasing and decreasing correspondingly. This result is somewhat different to that of Kondo et al in 1971 [29] who showed the size of C_3S to be unchanged – however here we see a marked increase in crystallite size at 6hrs and 11 days. It is difficult to develop any trends in the data without further complementary experimental techniques to confirm the size increase at these two times.

In comparison using the Scherrer formula to estimate crystallite size results in consistently smaller size values – this is expected because the Scherrer formula doesn't take into account the effect of lattice strain on peak broadening, and hence overestimates the peak broadening due to crystallite size causing the crystallite size to be underestimated .It does however follow broadly similar trends to the WH size: decreasing initially with the low value at 3hrs before increasing slightly to around 0.991 at 1 day and then more or less staying a steady size until a marked increase at 11days.

Graph 5.4: shows the progression of average C_3S crystallite size and lattice strain as

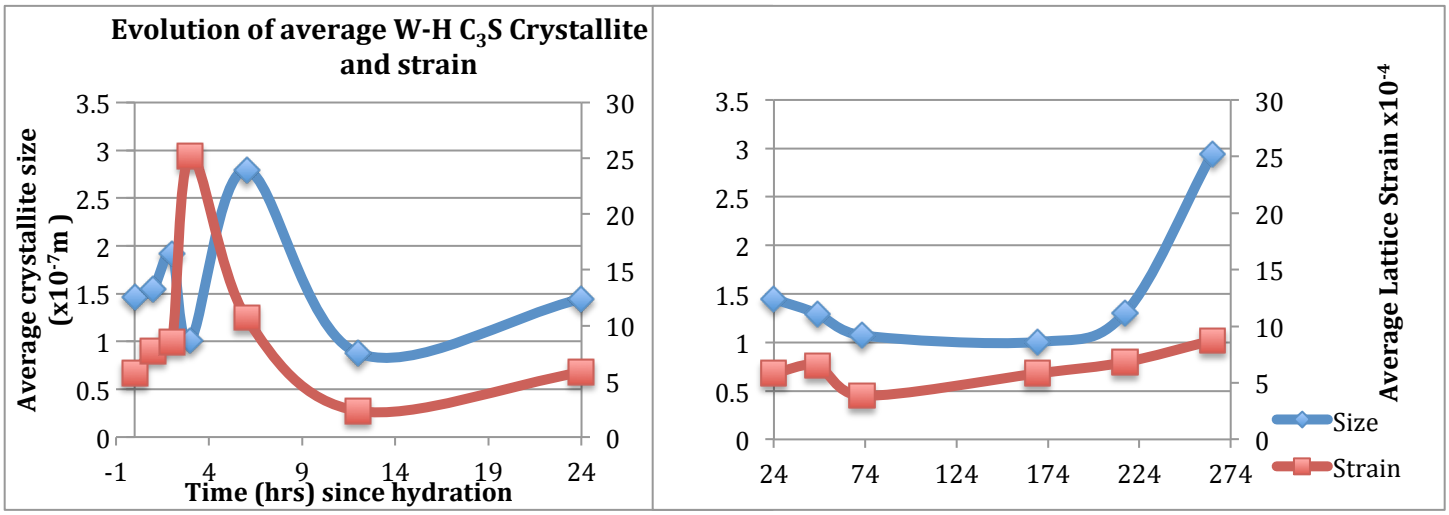

5.2.2 Phase identification

The PDXL autosearch function correctly identifies the unhydrated C_3S diffraction pattern correctly as Hatrurite ($Ca_9 O_{15} Si_3$). Very slow reaction rate compared with C_3A . There is an unidentified peak emerging from what appears to be an amorphous hump in the background intensity at around 7°. C_3S peaks are only slightly reduced at 1hr hydration as shown in diffractogram 5.10

Diffractogram 5.10: The peak at 7° grows while other peaks decrease in intensity.

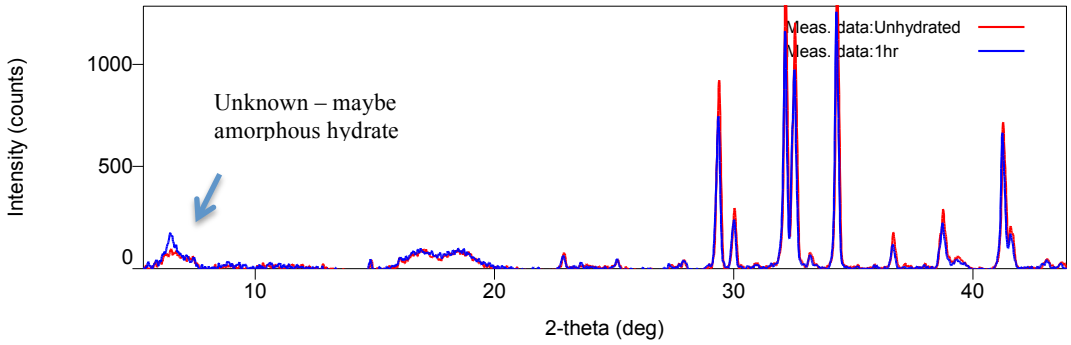

Diffractogram 5.11: The first indication of hydrate formation is at 12hrs with the appearance of a peak at 17.9° representing portlandite.

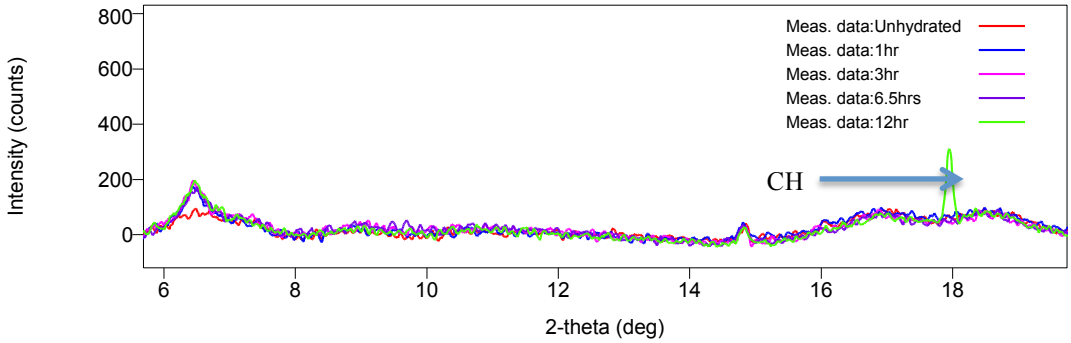

Diffractogram 5.12: The 17.9° CH peak reaches its maximum intensity at 24hrs and at 24hrs there is an additional portlandite peak that emerges at 2θ=33.9°

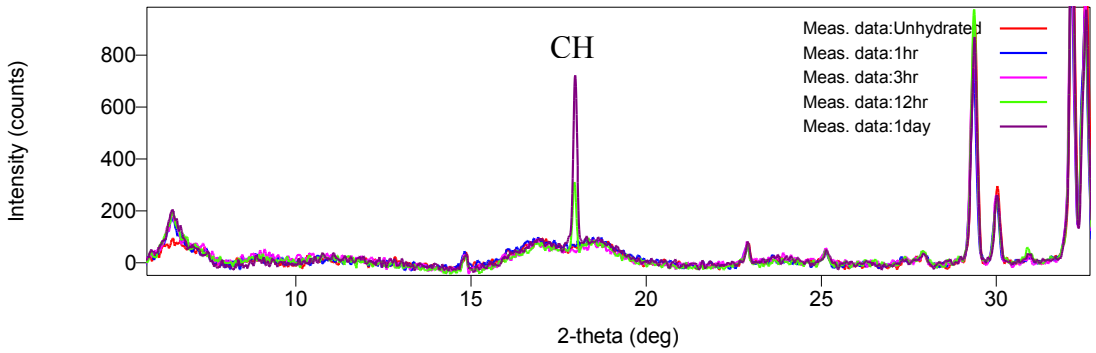

Diffractogram 5.13:CH peak at 33.9° emerges at 24hours and grows as indicated in graph

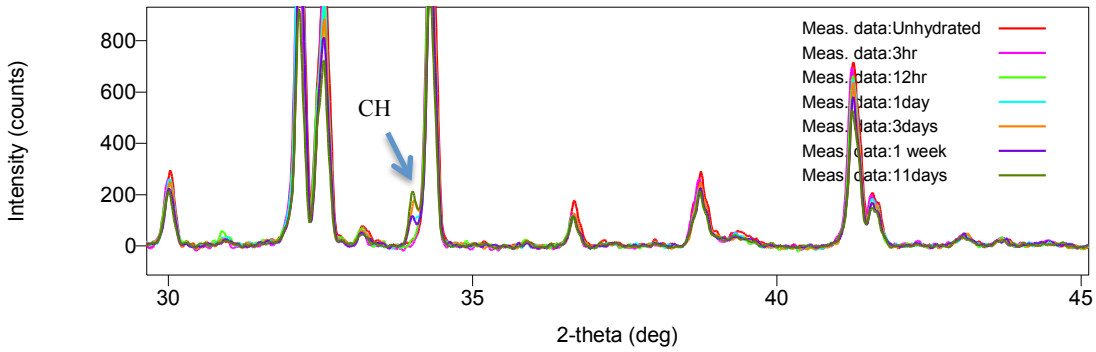

C_3S intensity decreases immediately on hydration, albeit slowly and there is a delay before CH forms: either it's taking a long time for the C_3S to hydrolyze and calcium and hydroxide ions to supersaturate in order for CH to finally crystallize out, or this could indicate an intermediate phase causing the delay, perhaps an amorphous C-S-H coating the C_3S, causing reduced hydrolysis and a diffusion limited reaction. Would require more measurements at closer time intervals and use of TEM/SEM to see the phases microscopically to confirm this.

5.2.3: Rate of peak growth and decline

Graph 5.5: Integrated intensity of C_3S and CH phases plotted as a function of time

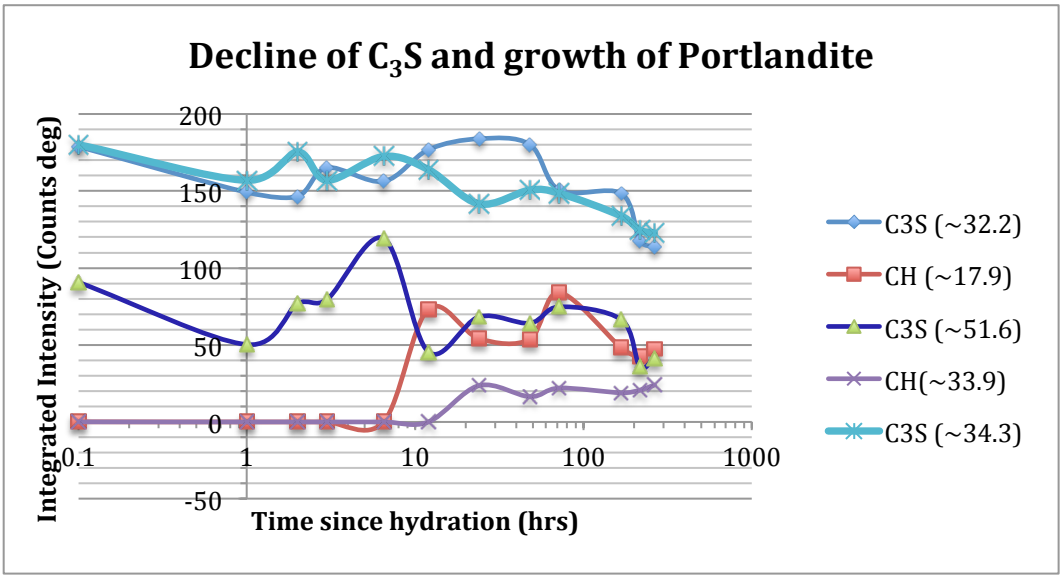

While the decreasing C_3S peaks do end up losing about 1/3 of their original intensity over the period of 11days hydrating (we know that 70% of C_3S reacts in the first 28 days[8]), the decline is rather variable for all C_3S peaks identified. The intensity decreases during the first hour of hydration but then increases again reaching a high point between 6.5 and 24 hours, followed by further demolition, then a slight plateau before further rapid decline. This may be a result of placing the sample back in the diffractometer for measurement, at a slightly different position to the previous measurement, where less sample has reacted, therefore making the C_3S appear to increase in intensity. The major portlandite peak at 17.9° emerges at 12hrs hydration i.e. directly following the rapid decline of C_3S peak 34.3° and 51.6°. The only other CH peak is observed at 24hours and this roughly corresponds to a second decline phase of the 51.6 peak.

5.3 Observations, conclusions and improvements

From observations of when hydration products appear in the diffraction patterns: We see a rapid hydrolysis of both C_3A and C_3S phases, which slows down at about 2hours in C_3A and 6hrs in C_3S. There is an clear induction period in the C_3S before products of portlandite crystallize out at 12hrs. No direct observation of amorphous C-S-H phases detected however can speculate that the presence of some undetected hydrate phase causing the prolonged induction period. The C_3A on the other hand reacts rapidly and hydrogarnet forms immediately, increasing its rate of formation at ~3hrs which is when C_3A begins to reach a steady state. There is no intermediate metastable calcium aluminate hydrate formation detected.

Unfortunately there is no defined trend relating to the average crystallite size to the lattice strain in C_3A due to the null result obtained from the WH plot as a result of the negative non-physical strain. However both the WH and Scherrer determination of the crystallite size for C_3A agree that the crystallite size decreases over time showing a total decrease from 1.50×10^{-7} m to 0.993×10^{-7}m according to WH (with which zero strain was found), from 1.931×10^{-7}m to 1.61×10^{-7}m from the graphical estimation using a horizontal fit through the WH plot, and appears to remain approximately the same size according to the Scherrer formula.

It is also difficult to obtain any solid trend from the C_3S data where the strain increases to a maximum at ~6hours, yet the CH crystallite hydrates don't appear until 12hrs, so this increase in strain is perhaps and indication of the presence of an this unidentifiable C-S-H phase with which C_3S is experiencing contact force, and is speculated to be causing the induction period before growth of CH at 12hours.

Therefore a nucleation and growth process appears to be the controlling step in general hydration, while diffusion through a hydrate layer controls the later steady state stages of the hydrates formed.

The average C_3S crystallite size appear to remain around the initial unhydrated value throughout except for an increase of 3 fold at 6hrs according to WH only and an increase

on the final measurement at 11days according to both WH and Scherrer calculations – these appear random. Would have to take further measurements and plot WH graphs relating to specific (hkl) planes to interrogate this issue further.

Observations of the growth rates of hydrate phases, portlandite and hydrogarnet from C_3A and C_3S respectively confirm the findings of previous research on mechanisms responsible for the hydration process; such as the Minard et al's findings [48] that the hydration rate is first under chemical control according to the dissolution of C_3A which first depends on the surface area of the grains and then the space available, given the amount of hydrates already precipitated into the porous capillary networkspace →i.e it's all about the amount of C_3A surface exposed to water. The rate will decrease when hydrates touch C_3A grains thereby minimizing the surface area exposed. And for C_3S, Young et al's work (1977) [21] is confirmed: The nucleation and growth mechanism whereby calcium and hydroxide ion concentrations rise to a high enough level for crystallization of CH to occur is supported by the C_3S findings which indicate that the induction period ends when CH crystallization commences (at 12hours according to my results, which is much longer than the usual ~3hours).

In conclusion, the effect of hydration on the OPC phases C_3S and C_3A is taken to be a continuing hydrolysis of the anhydrous grains that causes the ions liberated to saturate the solution and hydration products, Hydrogarnet Portlandite to crystallize out into the pore space previously occupied by water. This has the effect of increasing the micro strain of the sample as observed in the first 6hrs of C3S hydration.

The rapid formation of Hydrogarnet and CH between 6hrs and 24hrs indicates many microstructural change occurring and is represents of the acceleration period. The induction period lasts ~12 hrs in the C_3S sample, which is far slower than normal – this could be due to inadequate combining of the sample with water as water was pipetted onto samples rather than mixed thoroughly.

Improvements

Cement systems are complex and there are a vast number of analysis techniques that can be performed on such systems. Preparation could have been more precisely done – i.e. storing samples in an atmosphere-less environment, using a machine to perform powdering of particles and measure the size externally to check the results are on track.

A disadvantage of using XRD to monitor the hydration is the length of time that it takes to obtain a diffraction pattern with the appropriate count statistics for identification. A synchrotron radiation source would be required to obtain data fast enough for an investigation of the very early moments of hydration where an acquisition speed of minutes would be necessary! Other methods to enhance the time resolution of measurements and make them more "in-situ" could be using a more efficient detector or use of acetone to freeze the hydration in its tracks.
Also as the diffractometer had many other users taking various measurements, this may have altered the machine alignment slightly – adding a level of uncertainty to the measurements. Therefore it would be good to repeat the experiment with the improvements mentioned above and also make use of other experimental techniques, such as SEM, TEM and calorimetry in conjunction with the XRPD to estimate the crystallite size and strain and thereby provide confirmation of the XRPD findings. Also use of alterative analysis techniques such as the Warren-Averbach method for separating size and strain effects [48].

6. REFERENCES

[1] F. Lea, "Lea's Chemistry of Cement and Concrete", Arnold publishers, edited by Peter C. Hewlett , 4th edition, 1998 , Ch.1

[2] "What is the development impact of concrete?" Cement trust, http://cementtrust.wordpress.com/a-concrete-plan

[3] Scrivener, K. L. "The Concrete Conundrum". Chemistry World, March 2008, p. 62−66

[4] F. Lea, *"Lea's Chemistry of Cement and Concrete",* Arnold publishers, edited by Peter C. Hewlett , 4th edition, 1998, Ch.8

[5] Flatt. R. J, Roussel. N Cheeseman.C.R ,"Concrete: An Eco Material that Needs to be Improved.", Journal of the European Ceramic Society, 2012. 32; p.2787−2798.

[6] Lamour, V.H.R.; Monteiro, P.J.M.; Scrivener, K.L.; Fryda, H. "Microscopic studies of the early hydration of calcium aluminate cements", International Conference on Calcium Aluminate cement (CAC), Edinburgh, UK, 2001; p.169-180.

[7] M. Merlinia, G.Artioli, *"The early hydration and the set of Portland cements: In situ X-ray powder diffraction studies"* ,Powder Diffr., September 2007, Vol. 22, No. 3.

[8] H.F.W. Taylor, "Cement Chemistry", Thomas Telford, London, 2nd Ed., 1997, ch. 1.

[9] A.M.Neville, *"Properties of concrete",* Pearson Education Limited, 5th Ed., 2011, p.8 , table 1.1"Main compounds of Portland cement" .

[10] K.l. Scrivener, *"Options for the future of cement",* The Indian Concrete Journal, July 2014, Vol. 88, Issue 7, p. 11-21

[11] Mondal, P. and Jeffery, J.W. "The crystal structure of tricalcium aluminate, $Ca_3Al_2O_6$", Acta Cryst. 1975. B31, p.689-697.

[12] Jeffry, J.W.,"The crystal structure of tricalcium Silicate" Acta cryst. 1952, Vol. 5, p.26-35.

[13] F. Lea, *"Lea's Chemistry of Cement and Concrete",* Arnold publishers, edited by Peter C. Hewlett , 4th edition, 1998, Ch.6.

[14] H.F.W. Taylor, "Cement Chemistry", Thomas Telford, London, 2nd Ed., 1997, Ch.5.

[15]A.M. Neville, "Properties of Concrete", Pearson Education Limited, 5th Ed, 2011, p. 13.

[16] Mindess, S.; Young, J.F. (1981). Concrete. Englewood, NJ, USA: Prentice-Hall. ISBN 0-13-167106-5.

[17] Juilland, P., et al., "Dissolution theory applied to the induction period in alite hydration." Cement and Concrete Research, 2010. 40(6): p. 831-844.

[18] Gartner, E.M., et al., eds. "Structure and Performance of cements", 2nd edition, Spon Press ed. 2002. Ch.3.

[19] Garrault, S. and A. Nonat, "Hydrated Layer Formation on Tricalcium and Dicalcium Silicate Surfaces: Experimental Study and Numerical Simulations." Langmuir, 2001. 17(26): p. 8131- 8138.
[20] Jennings, H.M. "Aqueous Solubility Relationships for Two Types of Calcium Silicate Hydrate", J. Am. Ceram. Soc. (1986) 69, p. 614-618]
[21] Young et al. " Composition of solutions in contact with hydrating β-Dicalcium Silicate", J. Am. Ceram. Soc.,(1977), 60, p. 321-323.
[22] Jupe, A.C., et al., "Fast in situ x-ray-diffraction studies of chemical reactions: A synchrotron view of the hydration of tricalcium aluminate.", Physical Review B, 1996. Vol. 53(issue 22): p. R14697.
[23] Christensen, A.N et al "Formation of ettringite, $Ca_6Al_2(SO_4)_3(OH)_{12}.26H_2O$, AFt, and monosulfate, $Ca_4Al_2O_6(SO_4).14H_2O$, AFm-14, in hydrothermal hydration of Portland cement and of calcium aluminum oxide--calcium sulfate di-hydrate mixtures studied by in situ synchrotron X-ray powder diffraction." Journal of Solid State Chemistry, 2004. Vol. 177(issue 6): p. 1944-1951.
[24] Scrivener, K.L. and P.L. Pratt, "Microstructural studies of the hydration of C_3A and C_4AF independently and in cement paste.", Proc. Brit. Ceram. Soc, 1984. 35: p. 207-219.

[25] Pourchet, S., et al., "Early C_3A hydration in the presence of different kinds of calcium sulphate." Cement and Concrete Research, 2009. 39(11): p. 989-996.

[26]. K. FujII et al, " Kinetics of Hydration of Monocaldum Aluminate J. Am. Ceram. Soc., (1986), Vol. 69, issue 4, pp361-364.

[27] C. Suryanarayana and M.Grant Norton , "X-Ray Diffraction *A Practical Approach*", Plenum Press, New York. 1998.

[28]A.M. Neville, "Properties of Concrete", Pearson Education Limited, 5th Ed, 2011, p.20

[29] M. Diamon, S. Ueda and R. Kondo, "Morphological study on hydration of Tricalium silicate," Cement and Concrete Research, (1971) Volume 1, issue 4, pp. 391-401.

[30] Xianping . L , Robinson.I et al "In Situ Bragg Coherent Diffraction Imaging Study of a Cement Phase microcrystal during Hydration",2014, LCN, London.

[31] Maruyama. I et al , "Strain and thermal expansion coefficients of various cement pastes during hydration at early ages", Materials and structures, (2014), Vol. 47, issue 1-2, pp. 27-37

[32] Xi, Y. and Jennings, H.M., "Shrinkage of Cement Paste and Concrete Modeled by a Multiscale Effective Homogeneous Theory," Materials and Structures, (1997), Vol. 30, 329-339.

[33] Jinyao .C, D.D.L. Chung, "microstructural effect of the shrinkage of cement-based materials during hydration, as indicatated by electrical resistivity measurement", Cement and concrete Research, Vol. 34 (2004) pp. 1893-1897.

[34] F.J.Ulm, O.Coussy, "Modeling of thermo chemo mechanical couplings of concrete at early ages, Journal of Engineering Mechanics,} ASCE 121 (7) (1995), pp.785–794.

[35] F. Lea, *"Lea's Chemistry of Cement and Concrete",* Arnold publishers, edited by Peter C. Hewlett , 4th edition, 1998, Ch.4

[36] B.E. Warren , "X-Ray Diffraction", Dover Publications 1990, INC., New York (republication of the work originally published in 1969), Ch.2

[37] Ann. Phys. (Berlin) 524, No. 5, A83–A85 (2012)

[38] B.Fultz, J.Howe, springer-Verlag , "Transmission Electron Microscopy and Diffractometry of Materials" , Berlin Heidelberg, 2013, Ch.1

[39] H.F.W. Taylor, "Cement Chemistry", Thomas Telford, London, 2nd Ed., 1997, Ch.4.

[40] Himeda, Akihiro. "Multi-purpose X-ray diffractometer equipped with Kα1 optical system and ab initio powder crystal structure analysis", Rigaku journal, 2012.

[41] B.D. Cullity, S. R. Stock, "Elements of X-Ray Diffraction", 3 Edition, Prentice Hall, Upper Sadle River, NJ, USA, 2001.

[42] P. Scherrer, Göttinger Nachrichten Gesell., Vol. 2, 1918, p. 98.

[43] http://www.esu7.org/~leiweb/Staff/DSchmidt/Chemistry/Internet/States_of_Matter/Solids.htm (figure 3.1)

[44] IA R Stokes and A J C Wilson , "The diffraction of X rays by distorted crystal aggregates", Proc. Phys. Soc. (1944) Vol 56 p.174

[45] G.K. Williamson, W.H Hall, " X-ray Line Broadening from filed aluminium and wolfam", Acta. Metallurga, (1953) Volume 1, issue 1, pp 22-31.

[46] J.I Langford, “The breadth and shape of instrumental line profiles in high resolution powder diffraction” , J.appl.24 (1991) pp913-919

[47] Minard, H., et al., “Mechanisms and parameters controlling the tricalcium aluminate reactivity in the presence of gypsum.” Cement and Concrete Research, 2007. Vol. 37, issue 10, p. 1418-1426.

[48] B.E.Warren , B.L.Averbach, “The effect of Cold-Work Distortion on X-Ray Patterns”, J.appl.Phys. (1950), Volume 21, pp595

7. The Appendix

Appendix 7.1 : C_3A WH Plots

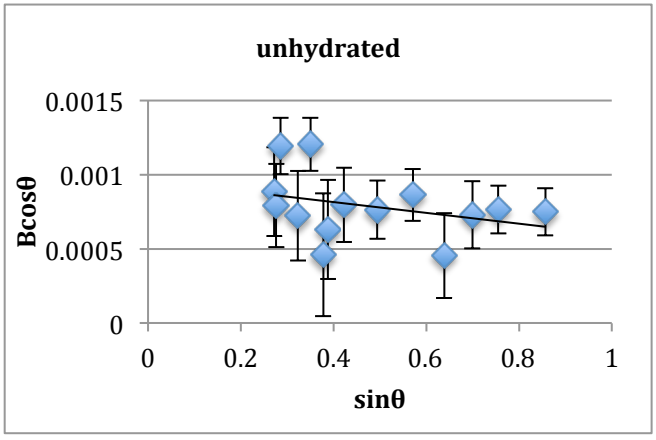

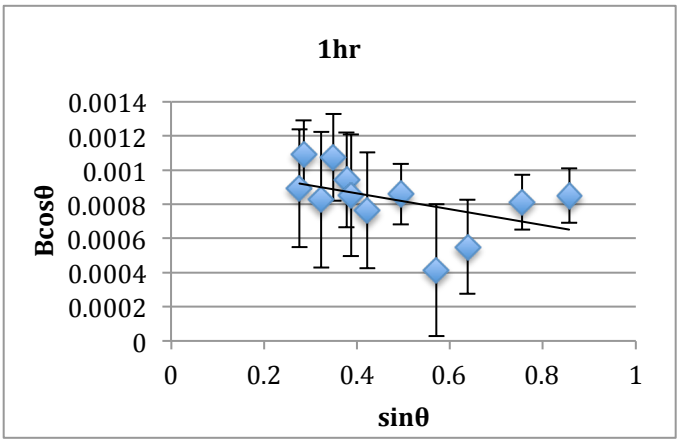

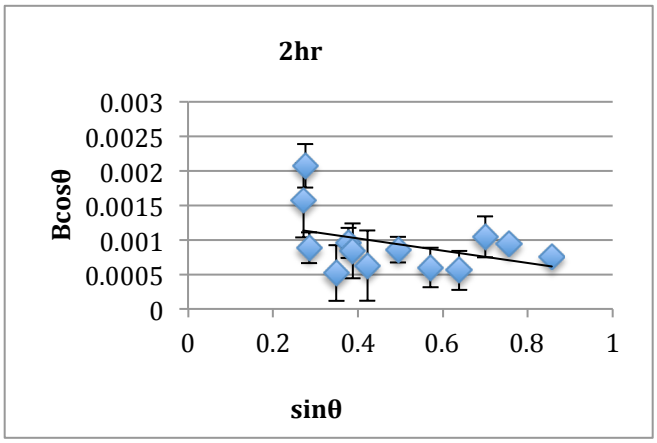

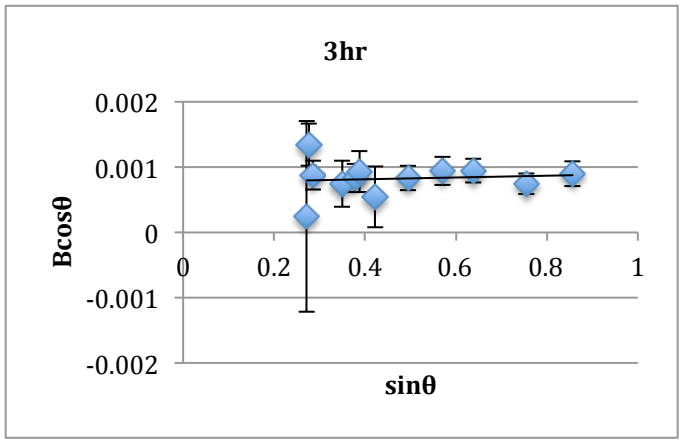

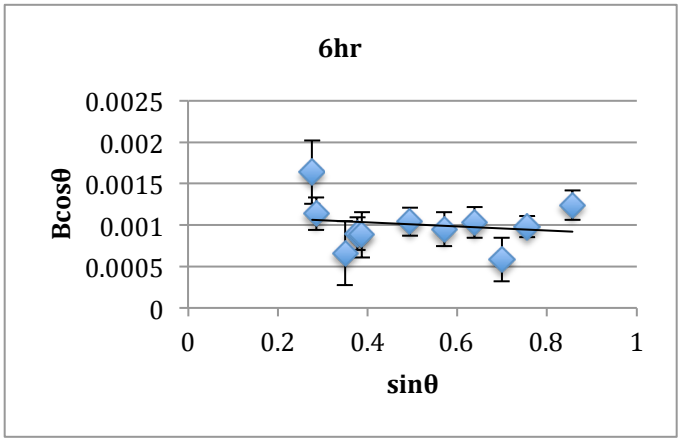

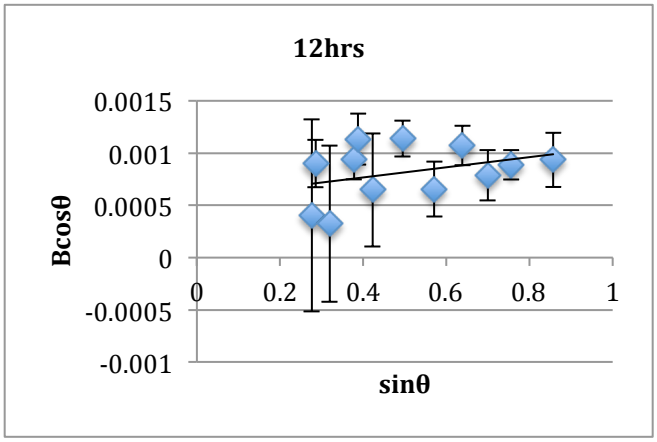

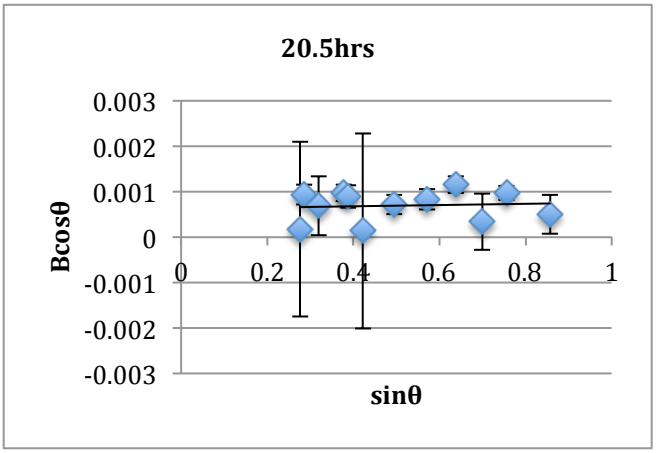
20.5hrs
0.003
0.002
0.001
0
-0.001
-0.002
-0.003
Bcosθ
0
0.2
0.4
0.6
0.8
1
sinθ

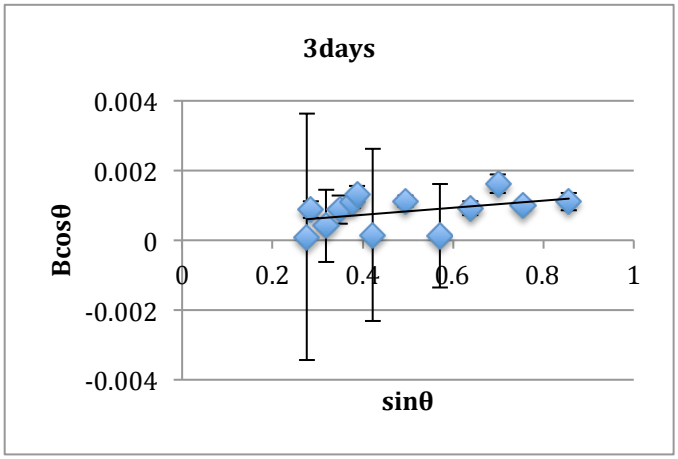
3days
0.004
0.002
0
-0.002
-0.004
Bcosθ
0
0.2
0.4
0.6
0.8
1
sinθ

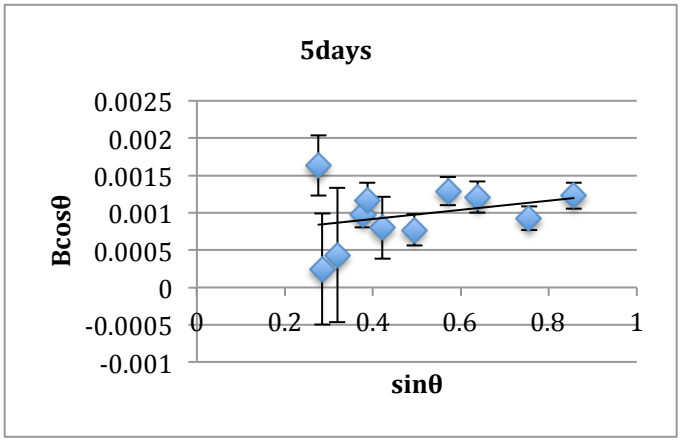
5days
0.0025
0.002
0.0015
0.001
0.0005
0
-0.0005
-0.001
Bcosθ
0
0.2
0.4
0.6
0.8
1
sinθ

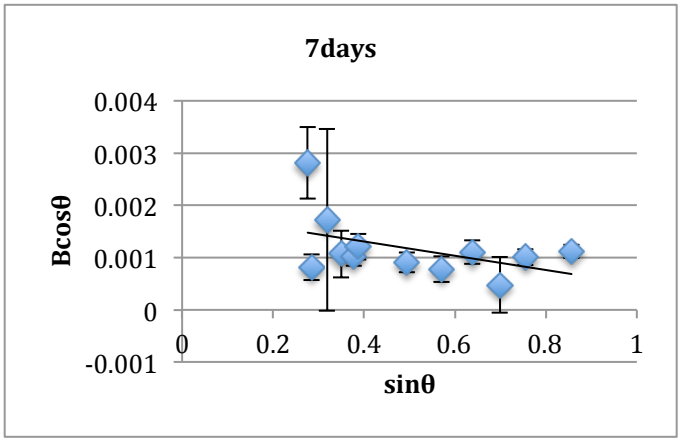
7days
0.004
0.003
0.002
0.001
0
-0.001
Bcosθ
0
0.2
0.4
0.6
0.8
1
sinθ

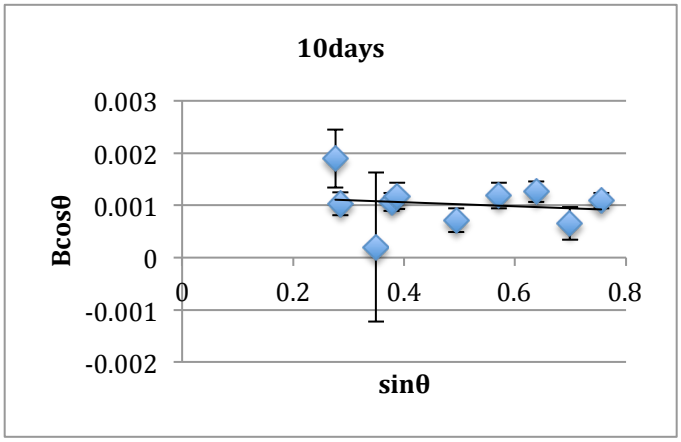
10days
0.003
0.002
0.001
0
-0.001
-0.002
Bcosθ
0
0.2
0.4
0.6
0.8
sinθ

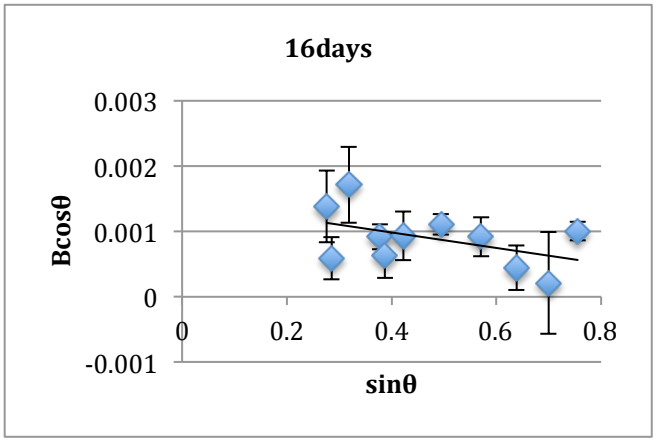
16days
0.003
0.002
0.001
0
-0.001
Bcosθ
0
0.2
0.4
0.6
0.8
sinθ

Appendix 7.2: C_3S WH Plots

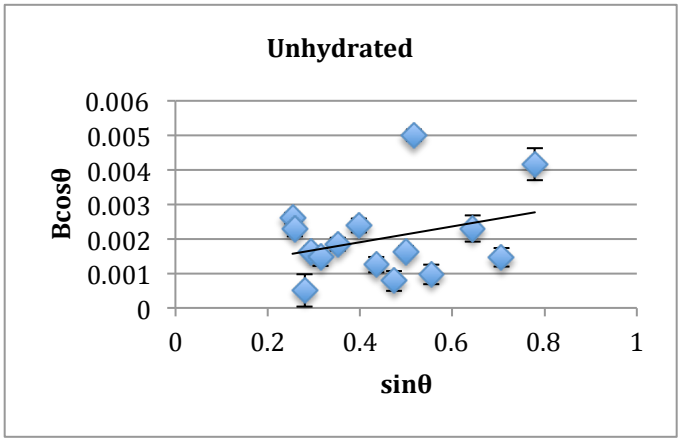

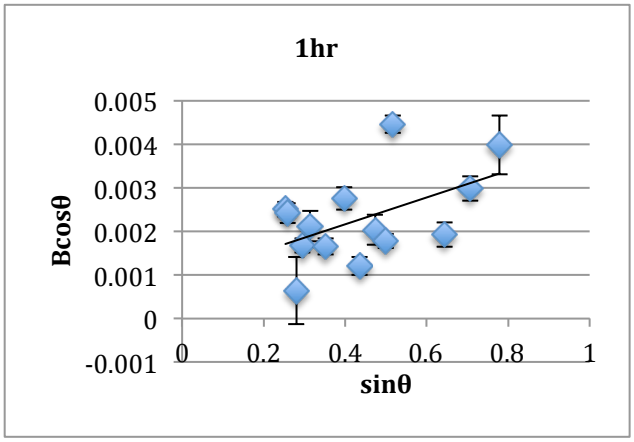

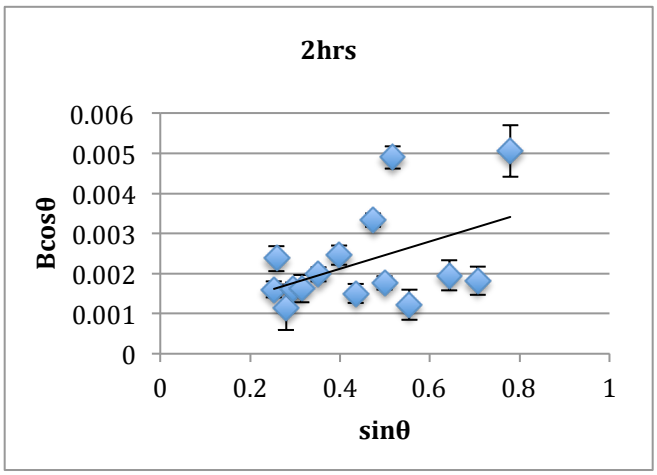

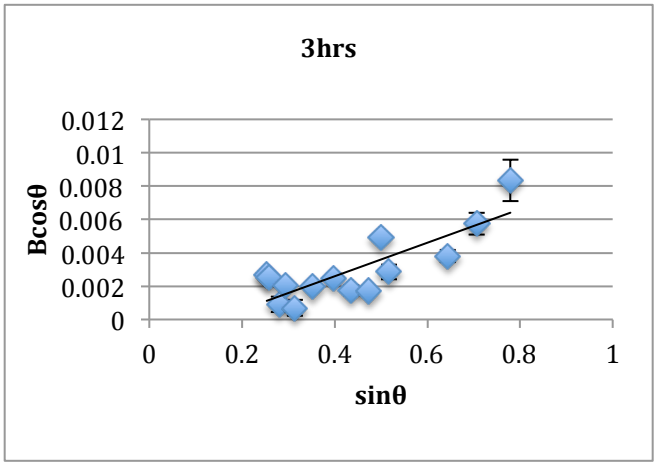

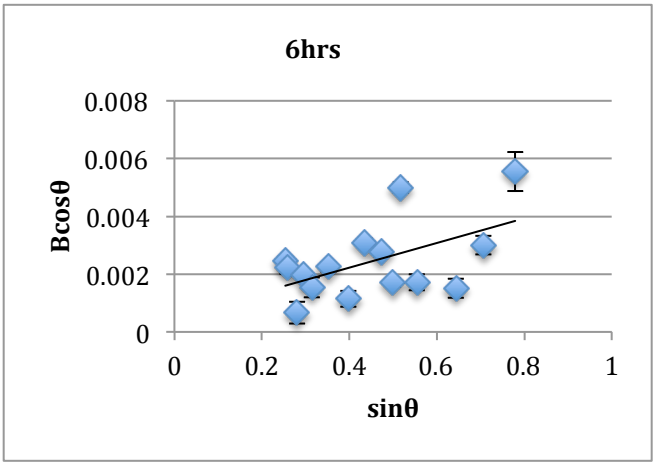

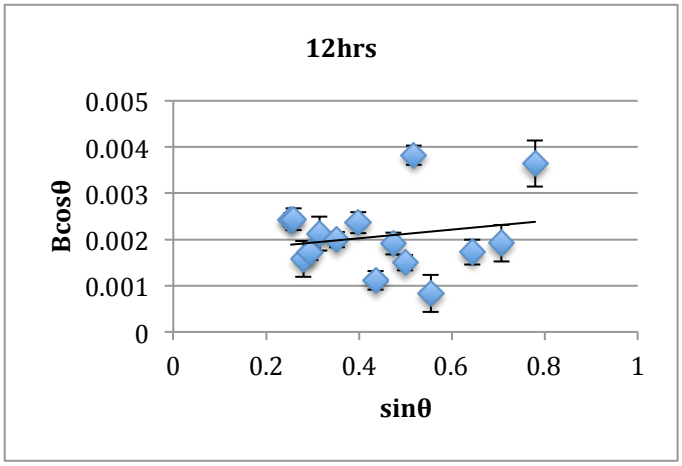

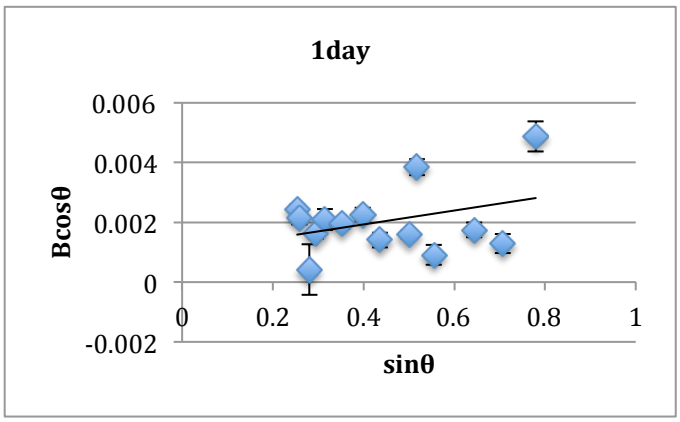
1day
Bcosθ
sinθ
0.006
0.004
0.002
0
-0.002
0
0.2
0.4
0.6
0.8
1

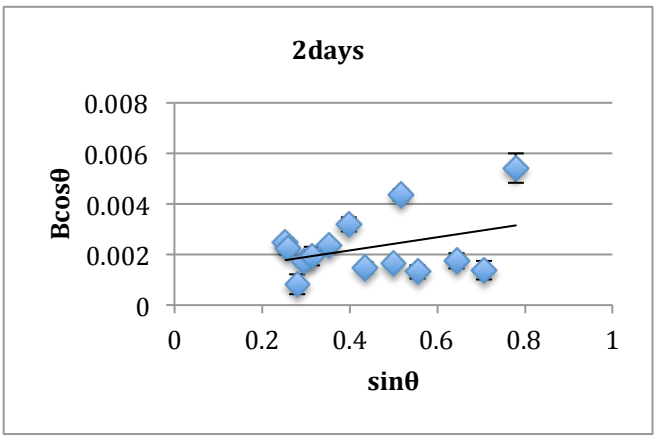
2days
Bcosθ
sinθ
0.008
0.006
0.004
0.002
0
0
0.2
0.4
0.6
0.8
1

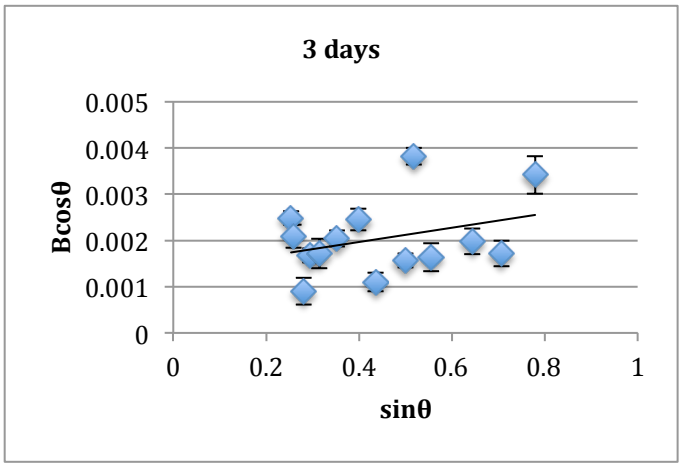
3 days
Bcosθ
sinθ
0.005
0.004
0.003
0.002
0.001
0
0
0.2
0.4
0.6
0.8
1

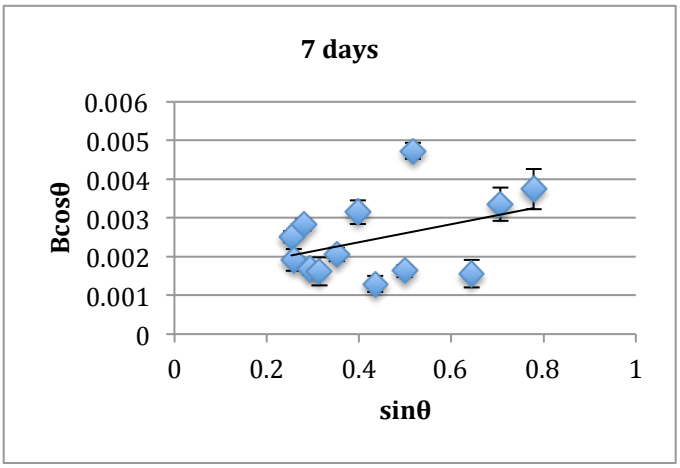
7 days
Bcosθ
sinθ
0.006
0.005
0.004
0.003
0.002
0.001
0
0
0.2
0.4
0.6
0.8
1

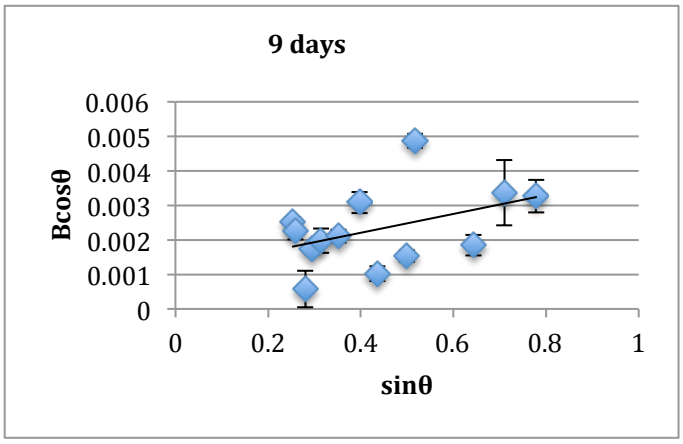
9 days
Bcosθ
sinθ
0.006
0.005
0.004
0.003
0.002
0.001
0
0
0.2
0.4
0.6
0.8
1

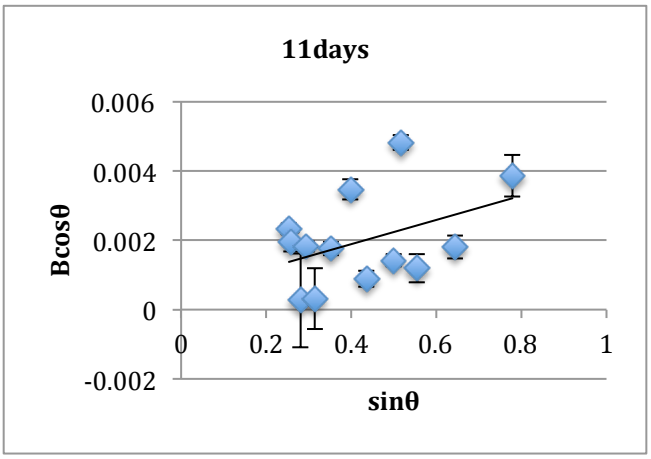
11days
Bcosθ
sinθ
0.006
0.004
0.002
0
-0.002
0
0.2
0.4
0.6
0.8
1

Appendix 7.3: Error propagation calculation for WH analysis

Errors contributing to 2θ consisted of the following: The estimated standard deviation given by the PDXL software.

There is a systematic error due to sample displacement which makes the diffracting surface deviate from the focusing circle, leading to peak shifts and asymmetric broadening at lower angles, given by: [38] .

$\Delta\theta = \frac{-D\ \cos\theta}{R}$ (in radians) (6.1)

D=displacement from the correct position

R= radius of the diffractometer circle (300mm for the smartlab)

Where the D is estimated to be 0.2mm . Specimen displacement can cause the diffraction peaks to shift to higher angles.

A systematic error is incurred as a consequence of the sample not following the curvature of the focusing circle and is given according to $\cos^2\theta$. Also potential axial divergence can cause the x-ray beam to diverge out of the plane of the focusing circle and is estimated by 0.1mm/170mm where 170mm is the distance between the beam emerging from the divergent slit and striking the sample. Axial divergence is controlled using soller slits (stacked plates that slice the incident beam into a stack of beams, each having low axial divergence). A detector slit between the sample and detector, controls equatorial divergence. The receiving slit defines the position of the detector. Equatorial divergence is eliminated using BB geometry which "gives well-defined diffraction angles for finite slit widths and beam divergences" [38].

Also it is important that the sample be made up of randomly orientated crystals, as preferred orientation can cause systematic errors in peak intensities

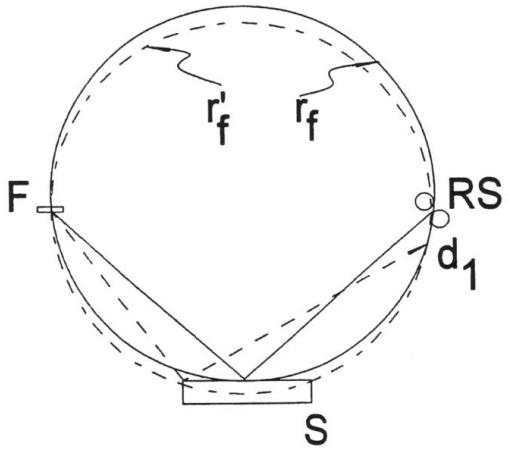

Figure 6.1 shows effect of sample misalignment on position of 2θ; the dashed line indicates deviation(r'_f) from the focusing circle (r_f). RS is the receiving slit to the detector and F the focusing slit from the x-ray source

The diagram above shows how 2θ position can vary when the height alignment is off; similar idea for flat specimen error – where the outer edges lie on another focusing circle (given by rf') and causes the diffracted intensity to appear at a lower 2θ value as indicated.

In taking an average of the measurement of the standard silicon Bragg peak positions taken at different points throughout the investigation, we can see that the average is a consistently 0.02° below the standard reference pattern values. Therefore the machine is perhaps making the measured Bragg angles of the cement samples less than they should be (possible accumulation of above mentioned error or intrinsic to the machine itself.

Table 6.1: Silicon ref. sample Bragg peak values, from measurements taken throughout the project and average clearly 0.02 less than ref.

	Measured Silicon 2θ 's measured with associated estimated standard deviation (°)					
Measurement no.	28.44	E.S.D	47.30	E.S.D	56.12	E.S.D
1	28.4274	0.00200	47.2818	0.000757	56.1054	0.000714
2	28.4164	0.00144	47.2816	0.000870	56.0945	0.000768
3			47.2766	0.001130		
4	28.4138	0.00266	47.2747	0.001170	56.0992	0.001030
5	28.4164	0.00144	47.2816	0.000870	56.0945	0.000768
6	28.4189	0.00189	47.2812	0.000696	56.1005	0.000356
7	28.4167	0.00123	47.2828	0.001040		
8	28.4188	0.00200	47.2807	0.000504	56.1044	0.005120
Average 2θ (°)	28.42		47.28		56.10	

This apparent offset of 0.02° can also be seen when running the PDXL autosearch function. For example in identifying the unhydrated C_3A diffraction pattern as Calcium cyclo-hexaaluminate for which the 100% relative intensity Bragg peak should occur at 33.18°, but is measured at 33.2°, another peak representing 39.6% relative intensity of C_3A is measured at 59.3°, but the standard is 59.27° and the peak representing 38.61% relative intensity measured at 47.65° is given at 47.63° in the database. The d values are consequently ~0.001 angstroms off. Similarly peaks of hydrogarnet are ~0.03° less than the databasereference value attained

As a result of of this 2θ variation, I have added a shift error of 0.02° into the uncertainty around the 2θ measurement.

The error in the measured FWHM (β_o) comes from the estimated standard deviation given by PDXL variation plus the uncertainty in 2θ from changes to beam position on the sample according to sample height alignment variation given by equation (6.1)

The error associated with the FWHM of the Si measurements used to estimate the instrumental broadening, β_i , can be seen from a plot of the FWHM of si Bragg peaks measured at different times throughout data taking. This error can be attributed to slit divergence thereby affecting all measured FWHM's

Error on β_i estimated by taking the midway point between the maximum and minimum FWHM's attained over the course of the investigation, for 3 Bragg peaks angles and then averaging those values to give ± 0.00347.

Table 6.2: showing the estimated uncertainty in β_i FWHM

	Si bragg peaks (°)		
2θ	28.44	47.3	56.12
(Max-min)/2 fwhm	0.0025	0.0043	0.00325
Average (Δβi)	0.00347		

Graphs 6.1-6.3 indicate how the FWHM of Si Bragg peaks varied over the course of data taking

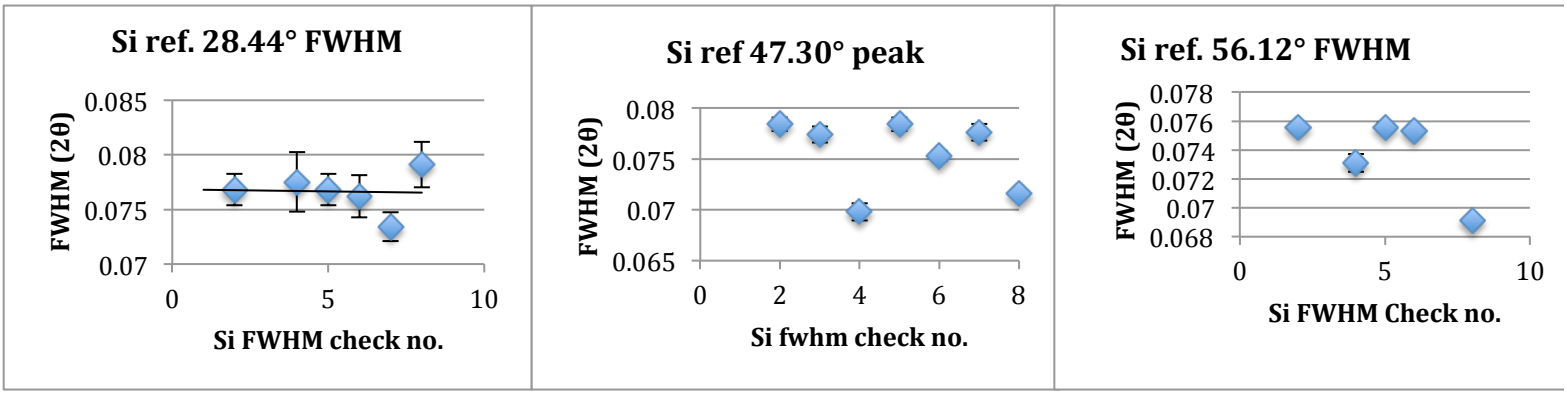

Now the instrumental broadening contribution to the individual peak widths of each diffraction pattern was found by plotting a FWHM correction curve using Si peaks (considered equivalent to instrumental broadening) and then subtracting the instrumental broadening contribution corresponding to each 2θ Bragg peak in the sample diffractograms. There was a human error in this subtraction of ± 0.0025°. Therefore the total error attributed to β_i =0.0025+0.00347 = 0.00597.

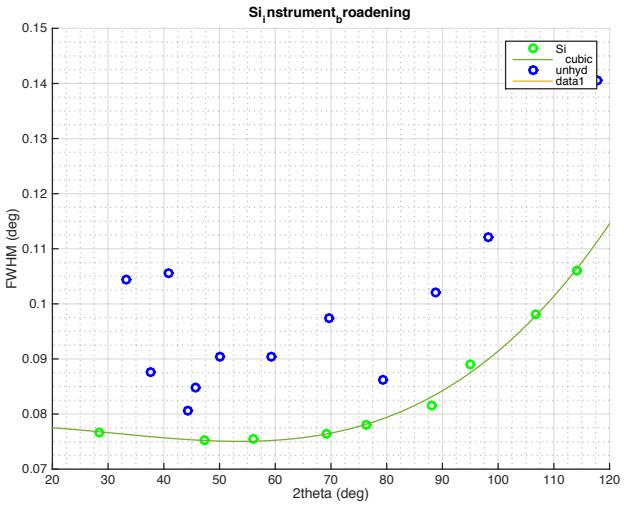

Figure 6.2 : instrumental profile derived from si reference sample, plotted in matlab

the crystallite size broadening is most evident at larger 2θ angles…for high angle diffraction peaks; both methods increase the instrumental fwhm

Hence the error associated with the β_r, the broadening attributed purely to the sample, given by equation (3.12) – and subsequently errors associated with the W-H plots are calculated through a series of error propagation calculations as follows:

$$\beta_r^2 = \beta_o^2 - \beta_i^2 \quad (6.1)$$

$$\beta_r = \sqrt{\beta_o^2 - \beta_i^2} \quad (6.2)$$

Let $A = \beta_o^2 - \beta_i^2$ (6.3)

$\rightarrow \beta_r = \sqrt{A}$ (6.4)

Errors found in ${\beta_o}^2 and\ {\beta_i}^2$ via error propagation rules:

$$\frac{\Delta\beta_o^2}{\beta_o^2} = 2\left(\frac{\Delta\beta_o}{\beta_o}\right)\beta_o^2 \quad (6.5)$$

Similarly for ${\beta_i}^2$

$$\frac{\Delta\beta_i^2}{\beta_i^2} = 2\left(\frac{\Delta\beta_i}{\beta_i}\right)\beta_i^2 \quad (6.6)$$

Then

$$\Delta A = \sqrt{\left(\Delta{\beta_o}^2\right)^2 + \left(\Delta{\beta_i}^2\right)^2} \quad (6.7)$$

and finally $\Delta\beta_r = \beta_r\left(\frac{1}{2}\frac{\Delta A}{A}\right)$

The error on the y-axis of w-h plot is then found using the partial derivative propagation rule for uncertainty in a function of several variables:

Let $Z=\beta_r \cos\theta$ (6.8)

$$\Delta(Z) = \sqrt{\left(\frac{\partial Z}{\partial \beta_r}\right)^2 (\Delta\,\beta_r)^2 + \left(\frac{\partial Z}{\partial \cos\theta}\right)^2 (\Delta\cos\theta)^2} \quad (6.9)$$

Where $\Delta\cos\theta = \sin\theta\Delta\theta$ from partial derivative error propagation. Hence the errors on the horizontal axis $\Delta\sin\theta = \cos\theta\,\Delta\theta$. But it is the vertical y-axis errors that show the linear fit in the C_3A WH plots can be taken as a null result and fit with horizontal lines. Errors can be seen displayed the C3A and also in the C3S W-H plots in appendix 6.1 and 6.2